Chemical Engineering Journal 535 (2026) 175211

Contents lists available at ScienceDirect

Chemical Engineering Journal

journal homepage: www.elsevier.com/locate/cej

A hybrid simulated moving bed/pressure swing adsorption process for methane and nitrogen separation

Rafael O.M. Dias [a,*], Alexandre F.P. Ferreira [a], Alírio E. Rodrigues [a], Ana M. Ribeiro [a,*]

[a] LSRE-LCM, ALiCE, Faculty of Engineering, University of Porto, Rua Dr. Roberto Frias, 4200-465, Porto, Portugal

ARTICLE INFO

Keywords:
Adsorption
CH_4/N_2 separation
Gas-phase simulated moving bed
SMB/PSA hybrid process

ABSTRACT

The conventional gas-phase simulated moving bed (SMB) process is a promising alternative to the cryogenic distillation for the rejection of nitrogen from methane streams for small-scale applications. However, one of its biggest disadvantages is the need to separate the downstream products, in this case, methane and nitrogen, from the desorbent species that is used in the process to regenerate the adsorbent. To overcome this, one can use a combination of pressure swing adsorption (PSA) steps and displacement chromatography to remove the adsorbed phase from the solid material. This way, the desorbent gas can be removed from the process.

This work presents an *in-silico* study of such hybrid SMB/PSA process. A parametric study was also conducted to observe the effect of different operating conditions on the performance and improve the process.

This advanced technique was able to produce high purity methane and nitrogen streams, meeting stricter purity requirements for methane streams (97%) and achieving high nitrogen purity (99%). Partial recovery of the purge outlet stream as heavy product gas enables an increase in methane recovery and productivity, reaching values of up to 97.3% and 11.5 $kg \cdot m_{ads}^{-3} \cdot h^{-1}$, respectively. Optimising the purge flow leads to a higher nitrogen recovery and productivity. Maintaining very low desorption pressures (0.1 bar) was found necessary to achieve a good process performance, leading to higher power consumption (503.0 $W \cdot h \cdot kg_{CH4}^{-1}$).

1. Introduction

The separation of methane from nitrogen is a critical step in upgrading low-quality unconventional methane sources, which often contain high concentrations of N_2 that significantly reduce the heating value of the gas stream [1]. Depending on the unconventional gas source, the nitrogen content in the methane gas streams varies. For coalbed methane, CH_4 content can go as low as 60% [1]. In landfill gas, which is produced from the anaerobic decay of waste, N_2 content can range from 5 to 25%, especially when air infiltrates during active gas extraction at subatmospheric pressures, which is necessary to ensure higher CH_4 recovery and to avoid its release in the atmosphere [2]. This way, nitrogen must be removed to meet pipeline specifications or for liquefaction processes [1]. Efficient and cost-effective separation techniques are therefore necessary to maximize methane recovery and minimise environmental and economic costs.

Currently, the predominant method for CH_4/N_2 separation is cryogenic distillation. This technique exploits the difference in boiling points between methane (−161.5 °C) and nitrogen (−195.8 °C), allowing for their separation through fractional distillation at cryogenic temperatures [3]. The process typically involves compressing and cooling the gas mixture to liquefy the components, followed by staged separation in a distillation column [3]. Depending on the nitrogen content, a process with multiple distillation columns may be necessary [3]. While cryogenic distillation offers high separation efficiency, it is energy-intensive due to the low temperatures required and economically viable mainly for larger-scale applications (with flow rates above 4.9 $m^3 \cdot s^{-1}$) [4].

Adsorption-based separation of CH_4 and N_2 has emerged as a promising alternative to cryogenic distillation, particularly for small- to medium-scale applications. Due to the similar molecular sizes and kinetic diameters of CH_4 (3.8 Å) and N_2 (3.64 Å), the separation relies on the different adsorption affinity toward the stationary phase, diffusivity or tailored adsorbents with tuned pore size. Among the different materials utilised for this separation, carbon molecular sieves and titanosilicates have shown effective kinetic-based separation by exploiting the faster diffusion of N_2 over CH_4, producing methane at a high pressure [5–9]. On the other hand, equilibrium-based systems using activated carbons and metal-organic framework (MOF) materials generally favour

* Corresponding authors.
E-mail addresses: rmdias@fe.up.pt (R.O.M. Dias), apeixoto@fe.up.pt (A.M. Ribeiro).

https://doi.org/10.1016/j.cej.2026.175211
Received 16 October 2025; Received in revised form 2 January 2026; Accepted 12 March 2026
Available online 15 March 2026

CH_4 due to its higher polarizability and stronger interaction with the adsorbent surface [10–12]. As a result, the CH_4-rich product must be recompressed before being injected into the pipeline, adding to operational costs. This way, the choice between kinetic and equilibrium PSA depends on the specific application, with both approaches being found at an industrial scale [13,14].

In our previous works, the conventional gas-phase SMB process was shown to be a promising alternative to cryogenic distillation for the rejection of nitrogen from methane streams [15–17]. However, one of its biggest disadvantages is the need to separate the downstream products, in this case, methane and nitrogen, from the desorbent species that is used in the process to regenerate the adsorbent [18]. To overcome this, one can use a combination of pressure swing adsorption steps and displacement chromatography to remove the adsorbed phase from the solid material. This way, the desorbent gas can be effectively removed from the process.

The combination of the simulated moving bed technology with pressure swing adsorption has been reported in the literature for several gas-phase applications. LaCava and McKeigue first patented a continuous pressure difference-driven SMB process requiring no eluent [19]. Rothchild later patented a "pressure swing chromatography" process for selective adsorption of nitrogen from air, achieving high purity and nearly 100% yield through pressure-induced desorption [20]. Cheng and Wilson published two patents for separating propylene from a C3 hydrocarbon mixture by SMB with vacuum swing adsorption, achieving high-purity propylene at a high recovery rate [21,22]. Rao et al. modelled a hybrid SMB/PSA process to separate propane/propylene mixtures, achieving complete separation of the C_3 mixture with high productivity (100–300 $mol \cdot kg^{-1} \cdot h^{-1}$) under high vacuum conditions of 0.01 kPa [23]. Kostroski and Wankat researched the separation of diluted enantiomeric enflurane in a nitrogen carrier gas by coupling the gas-phase SMB technology with pressure swing adsorption (PSA) [24]. In 2009, the authors applied this system for the separation of concentrated binary gases, more specifically, the separation of a H_2/CH_4 mixture [25]. More recently, Qian et al. introduced an improved VPSA with SMB operation using activated carbon (AC) beads for CH_4/N_2 separation. In this experimental work, the authors reported enhanced CH_4 purity and recovery compared to PSA processes, producing a high-purity CH_4 stream (99.99%) with a 98.6% recovery [26]. The authors also tested the performance of commercial coconut shell AC using the improved VPSA process [27]. Building upon their previous works, the authors investigated the use of a ZSM-5 zeolite in their pilot VPSA-SMB unit. The best run achieved a 99% purity CH_4 stream with increased recovery (99.6%), however, with a power consumption 10 $kJ.mol_{CH4}^{-1}$ higher than what was observed with the AC materials [28]. In 2025, Miao et al. modelled the improved VPSA process for the separation of CH_4/CO_2 mixtures [29].

This work intends to build upon the state-of-the-art research on hybrid systems and implement and model a pilot SMB/PSA hybrid process for the separation of an equimolar methane/nitrogen mixture. In this computational study, the *gPROMS* software was used to implement the simulation framework for the hybrid process. The obtained simulation results highlight the performance of the process under various operating conditions and allowed to define a strategy to predict the operating conditions that provide complete separation of the two components. A parametric study was conducted to investigate the influence of the key process parameters on the hybrid system's performance.

2. Theory

2.1. SMB/PSA hybrid process

In the hybrid SMB/PSA process, the regeneration zone, designated as Section I, is decoupled from the SMB, and the desorbent is replaced with a sequence of PSA steps that rely on pressure variations for the adsorbent regeneration.

While one column undergoes these PSA steps in section I, in parallel, the remaining columns operate in series and are divided into two zones, which operate at different flow rates and have different functions. In Section II, known as the displacement zone, located between the displacing gas inlet and the feed inlet, the heavy product acts as the eluent to enrich the beds in the more retained species through displacement chromatography. In the adsorption zone, Section III, located between the feed inlet and the light product outlet, the more retained species adsorbs preferentially to the solid material while the less retained species travels in the fluid flow direction, with the outlet stream being enriched in the latter. After a switching time, t^*, elapses, which corresponds to the duration of one step, the inlets and outlets shift in the gas flow direction, promoting continuous mass transfer between solid and fluid phases. After the switch, the column that ended the PSA sequence in section I becomes the last column of section III, while the first column of section II becomes the column in section I to begin the PSA sequence. During a complete cycle of the SMB/PSA hybrid process, each column undergoes a total number of steps corresponding to the number of columns in the unit. Since the PSA sequence runs simultaneously to the SMB part of the process, to maintain synchronous operation of the process, the total duration of the PSA sub-steps (blowdown, counter-current purge, and co-current pressurization) must be equal to the switching time of the hybrid process, *i.e.*, one step (Eq. (1)).

$$t^* = t_{\text{blow}} + t_{\text{pg}} + t_{\text{press}} \tag{1}$$

The PSA sequence is comprised of the counter-current blowdown sub-step, during which the pressure is reduced, leading to the desorption of the more retained species and producing it at the column outlet. This is followed by a counter-current purge sub-step, where any residual impurities are removed using the light product as the purge stream. Then, a co-current pressurization sub-step is employed to restore the operating pressure, using the light product, ensuring the column is prepared to produce the less retained species in the following step.

Fig. 1 shows a schematic of an SMB/PSA hybrid process for methane/nitrogen separation. An eight-column configuration was projected, with one column in Section I, two in Section II, and five in Section III (1–2-5 column configuration). The total number of columns was fixed at eight to remain consistent with the existing pilot-scale gas-phase SMB unit and to facilitate its future adaptation to hybrid SMB/PSA operation. The number of columns allocated to the adsorption zone is due to the low adsorption selectivity of CH_4/N_2, requiring a longer bed length to enhance the separation efficiency. Like the traditional SMB, the flow rate in each section of the SMB component of the process is given by the balance to the nodes, in SLPM.

$$Q_{\text{II}} = Q_{\text{Disp}} \tag{2}$$

$$Q_{\text{III}} = Q_{\text{II}} + Q_{\text{F}} \tag{3}$$

By integrating SMB with PSA, this hybrid approach enhances separation efficiency, eliminates the need for a desorbent, and reduces additional purification steps, leading to a more cost-effective and streamlined process.

2.2. Fixed-bed mathematical model

Once the study of equilibrium and the adsorption dynamics is complete, a mathematical model that is able to describe the dynamic behaviour of multicomponent adsorption inside a fixed-bed column can be implemented to design an SMB/PSA hybrid process, also taking into account the transport phenomena. This model was used to simulate the results obtained for the hybrid SMB/PSA cycles and compute the separation regions. The mass, momentum, and energy balance equations that encompass the mathematical model and the initial and boundary conditions are presented below. The proposed model assumes ideal gas behaviour of the bulk phase, plug flow with axial dispersion, no radial

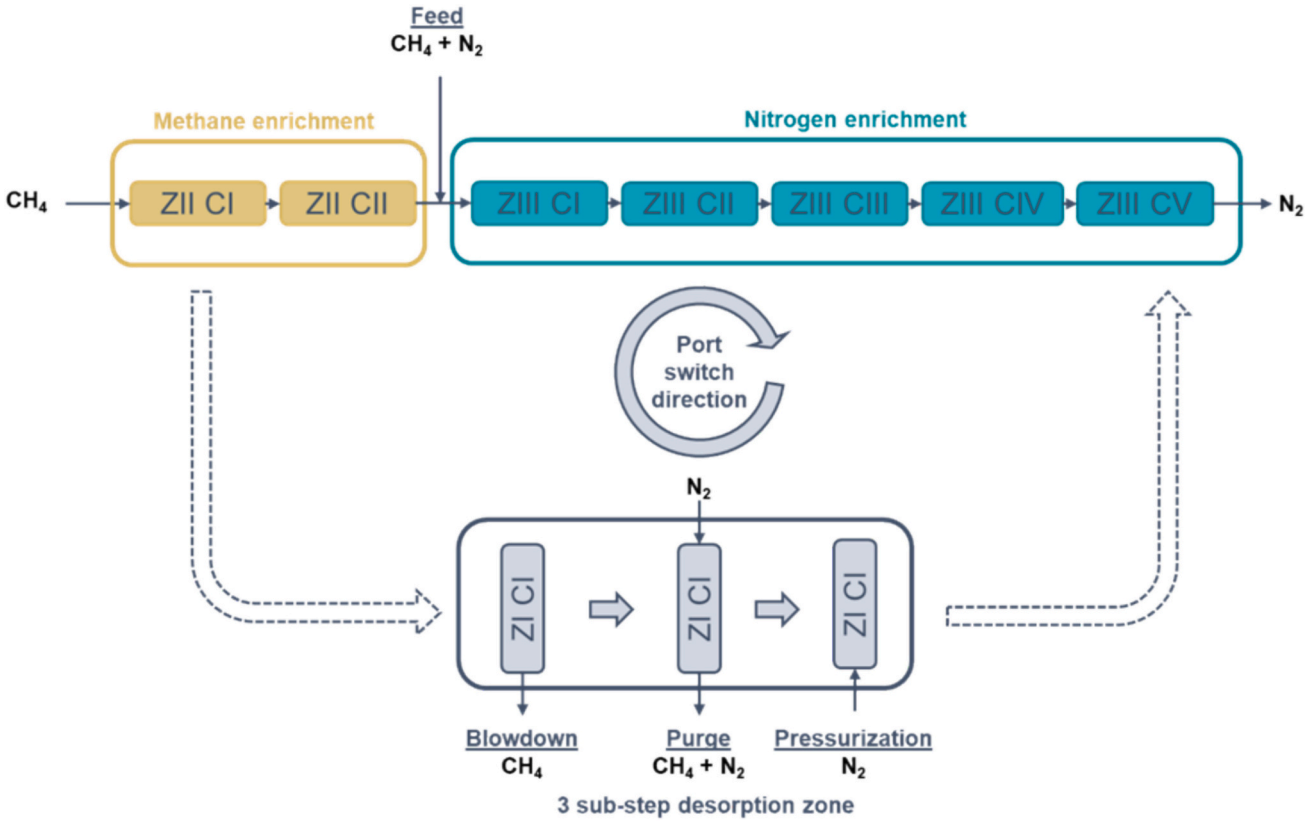

Fig. 1. Schematic of an SMB/PSA process with a 1–2-5 column configuration. Z corresponds to the section of the hybrid process, and C corresponds to the column.

mass, temperature, and velocity gradients, external mass and heat resistances expressed with the film model, bidispersed adsorbent particle with mass transfer resistances in both macropore and micropores expressed with the linear driving force (LDF) model, isothermal profile inside the particles and homogeneously packed columns with constant porosity [30]. Deviations from homogeneous packing may lead to broader concentration fronts and earlier breakthrough, although these effects are expected to be negligible for well-packed beds. This mathematical model has been previously validated for the conventional SMB process in a prior publication by our group [15], which includes adsorption equilibrium measurements, as well as dynamic breakthrough experiments for model validation, and cyclic SMB experiments compared directly with simulation results.

Mass balance to the gas phase

$$\frac{\partial}{\partial z}\left(\varepsilon D_{ax} C_{g,T}\frac{\partial y_i}{\partial z}\right) - \frac{\partial}{\partial z}\left(u_0 C_{g,i}\right) - \varepsilon\frac{\partial C_{g,i}}{\partial t} - (1-\varepsilon)a_p k_f\left(C_{g,i} - C_{s,i}\right) = 0 \quad (4)$$

where ε is the bulk porosity, D_{ax} is the axial dispersion coefficient, $C_{g,T}$ is the total concentration in the fluid phase, y_i is the molar fraction of component i, u_0 is the superficial velocity inside the column, $C_{g,i}$ is the concentration of component i in the fluid phase, a_p is the particle specific area, k_f is the film mass transfer coefficient and $C_{s,i}$ is the concentration of component i at the solid interface.

Mass balance to the solid phase at the macropore/mesopore scale

$$\frac{\partial \overline{C_{p,i}}}{\partial t} = k_{macro,i}\left(C_{s,i} - \overline{C_{p,i}}\right) - \frac{\rho_p}{\varepsilon_p}\frac{\partial \overline{q_i}}{\partial t} \quad (5)$$

where $\overline{C_{p,i}}$ is the averaged mole concentration of component i in the macropores, $k_{macro,i}$ is the macropore mass transfer resistance coefficient, ε_p is the particle porosity, ρ_p is the apparent particle density, and $\overline{q_i}$ is the average adsorbed amount of component i inside the particle per mass unit of solid.

Mass balance to the solid phase at the micropore level

$$\frac{\partial \overline{q_i}}{\partial t} = k_{micro,i}\left(q_i^* - \overline{q_i}\right) \quad (6)$$

where q_i^* is the adsorbed concentration in equilibrium with $\overline{C_{p,i}}$ and $k_{micro,i}$ is the mass transfer resistance coefficient at the micropore level.

Ideal gas law

$$P = \sum_{i=1}^{NC} C_{g,i} R_g T_g \quad (7)$$

Where P is the pressure evaluated locally at the axial position z, R_g is the ideal gas constant, T_g is the temperature of the fluid phase and NC is the number of components.

Momentum balance

$$-\frac{\partial P}{\partial z} = \frac{150\mu(1-\varepsilon)^2}{\varepsilon^3 d_p^2}u_0 + \frac{1.75(1-\varepsilon)\rho}{\varepsilon^3 d_p}u_0|u_0| \quad (8)$$

Where μ is the gas mixture viscosity, ρ is the gas mixture density and d_p is the particle diameter.

Energy balance to the gas phase

$$\frac{\partial}{\partial z}\left(\lambda\frac{\partial T_g}{\partial z}\right) - u_0 C_{g,T} c_P \frac{\partial T_g}{\partial z} + \varepsilon R_g T_g \frac{\partial C_{g,T}}{\partial t} - (1-\varepsilon)a_p h_f\left(T_g - T_s\right) - \frac{4h_w}{d_w}\left(T_g - T_w\right) - \varepsilon C_{g,T} c_V \frac{\partial T_g}{\partial t} = 0 \quad (9)$$

Where λ is the heat axial dispersion coefficient, T_g, T_s, T_w are the gas, particle, and wall temperatures, respectively, c_P and c_V are the specific heats at constant pressure and volume, respectively, h_f is the film heat transfer coefficient, h_w is the heat transfer coefficient between the fluid phase and the column wall, and d_w is internal wall diameter, equal to the bed diameter.

Energy balance to the solid phase

$$(1-\varepsilon)\left[\rho_p\sum_{i=1}^{NC}\overline{q_i}c_{V,i}+\rho_p\widehat{c}_{Ps}+\varepsilon_p\sum_{i=1}^{NC}\overline{C_{p,i}}c_{V,i}\right]\frac{\partial T_s}{\partial t}$$
$$=\rho_b\sum_{i=1}^{NC}$$
$$\times\sum_{k=1}^{N_{sites}}\left[\left(-\Delta H_{i,k}\right)\frac{\partial\overline{q_{i,k}}}{\partial t}\right]+(1-\varepsilon)a_p h_f\left(T_g-T_s\right)+(1-\varepsilon)\varepsilon_p R_g T_s\sum_{i=1}^{NC}\frac{\partial\overline{C_{p,i}}}{\partial t} \quad (10)$$

with $\widehat{c}_{Ps}$ being the solid specific heat per mass unit and ΔH_i being the enthalpic parameter of component i and site k.

Energy balance to the column wall

$$\rho_w\widehat{c}_{Pw}\frac{\partial T_w}{\partial t}=\alpha_w h_w\left(T_g-T_w\right)-\alpha_{wl}U(T_w-T_\infty), \quad (11)$$

$$\alpha_w=\frac{d_w}{e(d_w+e)};\alpha_{wl}=\frac{2}{(d_w+e)\ln\left(\frac{d_w+2e}{d_w}\right)} \quad (12)$$

where ρ_w is the wall density, $\widehat{c}_{Pw}$ is the wall specific heat at constant pressure (per mass unit), α_w is the ratio of the internal surface area to the volume of the column wall, α_{wl} is the ratio of the log mean surface area to the volume of the column wall, U is the overall heat transfer coefficient, T_∞ is the column surrounding temperature, and e is the wall thickness.

Flux equality at the solid surface

$$\frac{a_p k_f}{\varepsilon_p}\left(C_{g,i}-C_{s,i}\right)=k_{macro,i}\left(C_{s,i}-\overline{C_{p,i}}\right) \quad (13)$$

The transport parameters were obtained through the same correlations presented in the referenced work [15]. The molecular diffusivity and macropore diffusivity were estimated by the Chapman-Enskog and Bosanquet equations, respectively, which were used to determine the value of k_{macro} [31]. To determine the film mass and heat transfer coefficients and the axial heat dispersion coefficient, the Wakao and Funazkri correlations were used [32,33]. The axial mass dispersion coefficient was obtained using the Hsu and Haynes eq. [34].

The equations and estimated transport parameters were introduced into the *gProms* software to perform the required simulations. To discretise the axial coordinate, the orthogonal collocation on finite elements method (OCFEM), with second-order polynomials and 12 discretisation intervals, was used. The resulting system of ordinary differential equations was numerically solved with the Differential Algebraic Equation solver with Backward Differentiation Formulae (DAEBDF), with an absolute tolerance of 10^{-5}.

While performing the simulations, the mass balance to each component, as well as the global mass balance, were calculated to ensure there was mass conservation.

The initial and boundary conditions for the fixed-bed model are presented below.

Initial conditions

$$y_{N_2}=1 \quad (14)$$

$$y_{CH_4}=0 \quad (15)$$

$$\frac{\partial\overline{q_i}}{\partial t}=0 \quad (16)$$

$$\overline{C_{p,i}}=C_{g,i} \quad (17)$$

$$C_{g,T}=C_{inlet,T} \quad (18)$$

$$T_g=T_s=T_w=T_{inlet} \quad (19)$$

Boundary conditions for each bed

$z=0$, inlet:

$$u_{0,inlet}C_{inlet,i}=u_0C_{g,i}-\varepsilon D_{ax}C_{g,T}\frac{\partial y_i}{\partial z} \quad (20)$$

$$u_{0,inlet}C_{inlet,T}=u_0C_{g,T} \quad (21)$$

$$u_{0,inlet}C_{inlet,T}c_pT_{inlet}=u_0C_{g,T}c_pT_g-\lambda\frac{\partial T_g}{\partial z} \quad (22)$$

$z=L$, outlet:

$$\frac{\partial C_{g,i}}{\partial z}=0 \quad (23)$$

$$P=P_{outlet} \quad (24)$$

$$\frac{\partial T_g}{\partial z}=0 \quad (25)$$

The inlet for each bed is determined by the balance to the nodes for the SMB component of the hybrid unit.

2.3. SMB/PSA hybrid process modelling

To model and simulate the hybrid SMB/PSA process, in addition to the fixed-bed model presented above, it is necessary to model the nodes that interconnect the columns operating in SMB and account for the input and output streams of the process. These node balance equations are presented in Eqs. (26) to (31).

Displacement section node

$$u_{0,inlet,II}C_{inlet,i,II}=u_{0,Disp}C_{Disp,i} \quad (26)$$

$$u_{0,inlet,II}C_{inlet,T,II}=u_{0,Disp}C_{Disp,T} \quad (27)$$

$$u_{0,inlet,II}C_{inlet,T,II}c_pT_{inlet,II}=u_{0,Disp}C_{Disp,T}c_pT_{Disp} \quad (28)$$

Feed node

$$u_{0,inlet,III}C_{inlet,i,III}=u_{0,F}C_{F,i}+\left(u_{0,II}C_{g,i,II}\right)\big|_{z=L_{II}} \quad (29)$$

$$u_{0,inlet,III}C_{inlet,T,III}=u_{0,F}C_{F,T}+\left(u_{0,II}C_{g,T,II}\right)\big|_{z=L_{II}} \quad (30)$$

$$u_{0,inlet,III}C_{inlet,T,III}c_pT_{inlet,III}=u_{0,F}C_{F,T}c_pT_F+\left(u_{0,II}C_{g,T,II}c_pT_{g,II}\right)\big|_{z=L_{II}} \quad (31)$$

Also, the regeneration step of the SMB/PSA hybrid process involves a sequence of pressure swing sub-steps. Each sub-step is described by the fixed-bed dynamic model presented before with different boundary conditions, which depend on the characteristics of that sub-step. As such, coupled with the fixed-bed model, and the interconnection equations presented, the boundary conditions employed for each of the PSA sub-steps are given by the following equations:

Counter-current blowdown sub-step.

$z=L$:

$$\frac{\partial C_{g,i}}{\partial z} = 0 \tag{32}$$

$$u_0 = 0 \tag{33}$$

$$\frac{\partial T_g}{\partial z} = 0 \tag{34}$$

$z = 0$, outlet:

$$\frac{\partial C_{g,i}}{\partial z} = 0 \tag{35}$$

$$P = P_{outlet} \tag{36}$$

$$\frac{\partial T_g}{\partial z} = 0 \tag{37}$$

Counter-current purge sub-step (with the light product):
$z = L$, inlet:

$$u_{0,inlet} C_{inlet,i} = u_0 C_{g,i} - \varepsilon D_{ax} C_{g,T} \frac{\partial y_i}{\partial z} \tag{38}$$

$$u_{0,inlet} C_{inlet,T} = u_0 C_{g,T} \tag{39}$$

$$u_{0,inlet} C_{inlet,T} c_P T_{inlet} = u_0 C_{g,T} c_P T_g - \lambda \frac{\partial T_g}{\partial z} \tag{40}$$

$z = 0$, outlet:

$$\frac{\partial C_{g,i}}{\partial z} = 0 \tag{41}$$

$$P = P_{outlet} \tag{42}$$

$$\frac{\partial T_g}{\partial z} = 0 \tag{43}$$

Co-current pressurization sub-step (with the light product)
$z = 0$, inlet:

$$u_{0,inlet} C_{inlet,i} = u_0 C_{g,i} - \varepsilon D_{ax} C_{g,T} \frac{\partial y_i}{\partial z} \tag{44}$$

$$P = P_{inlet} \tag{45}$$

$$u_{0,inlet} C_{inlet,T} c_P T_{inlet} = u_0 C_{g,T} c_P T_g - \lambda \frac{\partial T_g}{\partial z} \tag{46}$$

$z = L$:

$$\frac{\partial C_{g,i}}{\partial z} = 0 \tag{47}$$

$$u_0 = 0 \tag{48}$$

$$\frac{\partial T_g}{\partial z} = 0 \tag{49}$$

During the blowdown step, the outlet pressure (P_{outlet}) decreases exponentially over time, starting from the pressure at the end of column I of Section II at the end of the previous step and gradually reaching the blowdown pressure (P_{low}) due to the valve opening. In the case of the counter-current purge step, P_{outlet} is constant and is equal to P_{low}. For the co-current pressurization step, the inlet pressure (P_{inlet}) increases linearly over time, from P_{low} to the pressure at the end of Section III, P_{high}.

2.4. Performance parameters

The performance of the SMB/PSA hybrid cycles was evaluated according to methane (A) and nitrogen (B) purity, product recovery, and process productivity, which are defined by the following equations. These parameters were evaluated at cyclic steady state, using data from one step (from time 0 to time t^*).

The heavy product is obtained during the blowdown sub-step. This way, the purity can be calculated by the amount of A that exits the column during this sub-step, divided by the total amount that exits the column (Eq. (50)). The light product is produced at the end of Section III. As a result, the light product purity is obtained by dividing the amount of B that exits this column during a step, divided by the total amount that exits the column (Eq. (51)).

Also, a portion of the heavy product is utilised as displacement gas in Section II. Thus, the methane recovery can be obtained by subtracting the amount of methane used as displacement gas during the step from the amount of methane produced and dividing it by the amount of methane fed to the system (Eq. (52)).

The purge and pressurization sub-steps are performed with part of the nitrogen product as the inlet gas. This way, the nitrogen recovery is calculated by subtracting the amount of nitrogen used during these sub-steps from the amount of nitrogen produced during a step at the end of Section III and dividing it by the amount of nitrogen fed at the feed inlet (Eq. (53)).

Accordingly, the heavy and light component productivity can be obtained through Eqs. (54) and (55).

Heavy and light component purity (%)

$$Pu_A = \frac{\int_0^{t_{blow}} C_{A,blow} u_0 \big|_{z=0,I} dt}{\sum_{i=1}^{NC} \left(\int_0^{t_{blow}} C_{i,blow} u_0 \big|_{z=0,I} dt \right)} \times 100 \tag{50}$$

$$Pu_B = \frac{\int_0^{t^*} C_B u_0 \big|_{z=L_{III}} dt}{\sum_{i=1}^{NC} \left(\int_0^{t^*} C_i u_0 \big|_{z=L_{III}} dt \right)} \times 100 \tag{51}$$

Heavy and light component recovery (%)

$$Rec_A = \frac{\int_0^{t_{blow}} C_{A,blow} u_0 \big|_{z=0,I} dt - \int_0^{t^*} C_{A,disp} u_0 \big|_{z=0,II} dt}{\int_0^{t^*} C_{A,F} u_{0,F} \big|_{z=0,III} dt} \times 100 \tag{52}$$

$$Rec_B = \frac{\int_0^{t^*} C_B u_0 \big|_{z=L_{III}} dt - \int_0^{t_{pg}} C_{B,pg} u_0 \big|_{z=L_I} dt - \int_0^{t_{press}} C_{B,press} u_0 \big|_{z=0,I} dt}{\int_0^{t^*} C_{B,F} u_{0,F} \big|_{z=0,III} dt} \times 100 \tag{53}$$

Heavy and light component productivity ($kg_{A,B} \cdot m_{ads}^{-3} \cdot h^{-1}$)

$$Prod_A = \frac{\left[\int_0^{t_{blow}} C_{A,blow} u_0 \big|_{z=0,I} dt - \int_0^{t^*} C_{A,disp} u_0 \big|_{z=0,II} dt \right] \times M^A}{V_s t^*} \tag{54}$$

$$Prod_B = \left[\int_0^{t^*} C_B u_0 \Big|_{z=L_{III}} dt - \int_0^{t_{pg}} C_{B,pg} u_0 \Big|_{z=L_I} dt - \int_0^{t_{press}} C_{B,press} u_0 \Big|_{z=0,I} dt \right] \times M^B V_s t^* \tag{55}$$

To increase the methane recovery, it was considered the possibility of a fraction of the purge outlet stream being recovered as heavy product, while the methane purity is kept above the 97% specification. The fraction of the purge duration where the purged methane is recovered is defined as $t_{int,\,pg}$. This way, only the gas purged from $t_{int,\,pg}$ to t^* is considered as waste. In this case, the purity, recovery and productivity of the heavy component are calculated by the equations provided below.

Heavy component purity (%)

$$\mathrm{Pu}_A = \frac{\int_0^{t_{blow}} C_{A,blow}u_0\big|_{z=0,I}dt + \int_0^{t_{int,pg}} C_{A,pg,out}u_0\big|_{z=0,I}dt}{\sum_{i=1}^{NC}\left(\int_0^{t_{blow}} C_{i,blow}u_0\big|_{z=0,I}dt + \int_0^{t_{int,pg}} C_{i,pg,out}u_0\big|_{z=0,I}dt\right)} \times 100 \tag{56}$$

Heavy component recovery, with purge recovery (%)

$$\mathrm{Rec}_A = \frac{\int_0^{t_{blow}} C_{A,blow}u_0\big|_{z=0,I}dt + \int_0^{t_{int,pg}} C_{A,pg,out}u_0\big|_{z=0,I}dt - \int_0^{t^*} C_{A,disp}u_0\big|_{z=0,II}dt}{\int_0^{t^*} C_{A,F}u_{0,F}\big|_{z=0,III}dt} \times 100 \tag{57}$$

Heavy component productivity ($\mathrm{kg_A \cdot m_{ads}^{-3} \cdot h^{-1}}$)

$$\mathrm{Prod}_A = \frac{\left[\int_0^{t_{blow}} C_{A,blow}u_0\big|_{z=0,I}dt + \int_0^{t_{int,pg}} C_{A,pg,out}u_0\big|_{z=0,I}dt - \int_0^{t^*} C_{A,disp}u_0\big|_{z=0,II}dt\right] \times M^A}{V_s t^*} \tag{58}$$

As previously mentioned, a portion of the CH_4 produced during the blowdown sub-step is used to displace the adsorbed phase in Section II. This way, a compressor is required to raise the low-pressure gas to the higher pressure at the inlet of the first column. The power consumption of this compressor was calculated assuming adiabatic and single-stage compression. An efficiency of 80% was considered for the compressor. The compression power required for the displacement gas, W_{disp}, was determined with the following equation:

$$W_{disp} = \frac{1}{\eta} F_{disp} R_g T_{inlet} \frac{\gamma}{\gamma - 1}\left[\left(\frac{P_{out}}{P_{atm}}\right)^{\frac{\gamma-1}{\gamma}} - 1\right] \tag{59}$$

Where F_{disp} is the molar flow rate of the displacement gas, T_{inlet} is the inlet temperature, P_{atm} and P_{out} are the atmospheric pressure and outlet pressure, respectively, and γ is the ratio between the heat capacity of the gas mixture at constant pressure and the heat capacity of the gas mixture at constant volume, $\gamma = c_P/c_V$.For the blowdown sub-step, since sub-atmospheric pressures were used, a vacuum pump is necessary. For the vacuum pump, an efficiency of 60% was considered. In this case, multiple stages with equal pressure ratios, and negligible pressure drop between stages were considered. Also, the inlet temperature was assumed to remain constant across stages. For the calculation of the power consumption of the blowdown, W_{blow}, a similar equation is employed:

$$W_{blow} = \frac{1}{\eta} F_{blow} R_g T_{blow} \frac{\gamma}{\gamma - 1}\left[\left(\frac{P_{atm}}{P_{low}}\right)^{\frac{\gamma-1}{\gamma}} - 1\right] \tag{60}$$

Where η is the pump efficiency, F_{blow} is the average molar flow rate of the blowdown sub-step, and T_{blow} is the temperature of the blowdown sub-step.

The used of a vacuum pump during the purge step is also necessary. To obtain the power consumption of the purge sub-step, W_{pg}, the following equation was used:

$$W_{pg} = \frac{1}{\eta} F_{pg,out} R_g T_{pg} \frac{\gamma}{\gamma - 1}\left[\left(\frac{P_{atm}}{P_{low}}\right)^{\frac{\gamma-1}{\gamma}} - 1\right] \tag{61}$$

Where $F_{pg,out}$ is the average molar flow rate at the outlet during the purge sub-step, and T_{pg} is the temperature of the purge sub-step.

The total power consumption is then calculated by the sum of the power consumption obtained for each sub-step, considering only the time percentage each pump is on:

$$W_T = W_{disp} + \frac{t_{blow}}{t^*} W_{blow} + \frac{t_{pg}}{t^*} W_{pg} \tag{62}$$

3. Results and discussion

Table 1
Fitting parameters of the DSL model for N_2 and CH_4 adsorption equilibrium on the BPL activated carbon.

Species	$q_{m,i,1}$	$q_{m,i,2}$	$b_{0,i,1} \times 10^4$	$b_{0,i,2} \times 10^4$	$-\Delta H_{i,1}$	$-\Delta H_{i,2}$
	$\mathrm{mol \cdot kg^{-1}}$	$\mathrm{mol \cdot kg^{-1}}$	$\mathrm{bar^{-1}}$	$\mathrm{bar^{-1}}$	$\mathrm{J \cdot mol^{-1}}$	$\mathrm{J \cdot mol^{-1}}$
N_2	6.78	0.66	3.33	2.03	10,856	15,648
CH_4	4.72	0.40	1.76	2.98	16,310	20,595

For the simulations, the BPL activated carbon was selected as the stationary phase, as from a process design perspective, it showed a higher productivity per column volume when compared to the other two materials tested in our previous studies [15–17]. Also, the BPL material has been fully characterized in our earlier work [15] through adsorption equilibrium isotherms and dynamic breakthrough experiments, and the fixed-bed model presented in Section 2.2 has been validated *a priori*, providing a reliable basis for the present study.

This way, the previously determined DSL model parameters for CH_4 and N_2 were used to describe the pure component adsorption equilibria [15]. The model parameters are presented in Table 1. For the multi-component adsorption equilibrium prediction, the extended DSL model was utilised (Eq. (63)), where the affinity parameter, $b_{i,k}$, of component i in site k is given by the Van't Hoff Equation (Eq. (64)). Also, the characteristics of the adsorption beds considered for this study are presented in Table 2. The bed characteristics listed in Table 2 were kept identical for all columns and fixed throughout the simulations to ensure compatibility with the pilot-scale SMB unit previously studied, intended for future adaptation to hybrid SMB/PSA operation.

$$q_i = q_{m,i,1}\frac{b_{i,1}P_i}{1 + \sum_{j=1}^{NC} b_{i,1}P_j} + q_{m,i,2}\frac{b_{i,2}P_i}{1 + \sum_{j=1}^{NC} b_{i,2}P_j} \tag{63}$$

Table 2
Characteristics of the adsorption beds.

	Value	Unit
Mass (m)	36.0	g
Internal diameter (d_w)	2.15	cm
Bed length (L)	25.0	cm
Bed porosity (ε)	0.41	
Bulk density (ρ_b)	396.6	$\mathrm{kg \cdot m^{-3}}$

Table 3
Initial set of operating conditions (Case 1).

Operating conditions	Value
P / bar	1.52–2.15
T / K	298
y_F	N_2: 0.5 CH_4: 0.5
P_{high} / bar	1.52
P_{low} / bar	0.10
t^* / s	200
t_{blow} / s	100
t_{pg} / s	60
t_{press} / s	40
Q_{pg} / SLPM	0.1

Table 4
Transport parameter values used in the simulations for the hybrid process.

Parameter	Value
$D_{ax} \times 10^4$ / $m^2 \cdot s^{-1}$	2.0
$k_f \times 10^2$ / $m \cdot s^{-1}$	1.41
λ / $W \cdot m^{-1} \cdot K^{-1}$	0.16
h_f / $W \cdot m^{-2} \cdot K^{-1}$	24.9
$k_{macro,i}$ / s^{-1}	N_2: 36.2 CH_4: 36.4
$k_{micro,i}$ / s^{-1}	N_2: 2.78 CH_4: 1.70
U / $W \cdot m^{-2} \cdot K^{-1}$	40.4
h_w / $W \cdot m^{-2} \cdot K^{-1}$	126.3

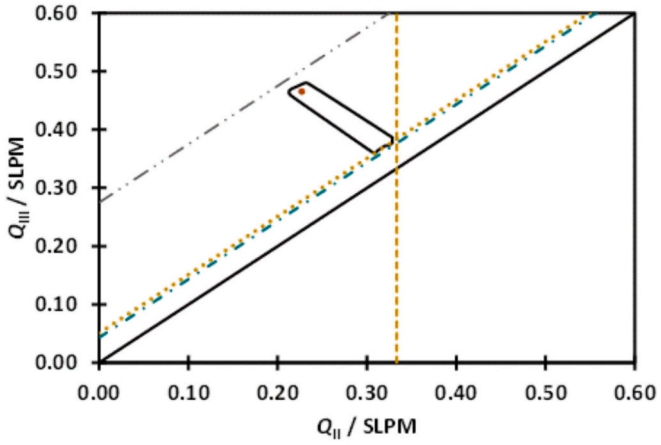

Fig. 2. Hybrid process separation region for CH_4/N_2 separation using BPL determined with the complete model, with a 1–2-5 configuration, for the initial set of operating conditions presented in Table 3, and heavy and light component purities of 97 and 99%, respectively (full black line). The yellow lines represent the displacement gas (dashed line) and feed flow rate (dotted line) restrictions for positive CH_4 productivity. The teal line represents the feed flow rate restriction for positive N_2 productivity (dash-dot line). The slanted grey line represents the maximum feed flow rate constraint obtained through the equilibrium theory (dash-double-dot line). The point (•) represents the operating conditions for Case 4.

$$b_{i,k} = b_{0,i,k} \exp\left(\frac{-\Delta H_{i,k}}{RT}\right) \tag{64}$$

Where $q_{m,i,k}$ is the saturation capacity, $b_{0,i,k}$ is the adsorption affinity constant at infinite temperature and $\Delta H_{i,k}$ is the enthalpic parameter for component i and site k.

The initial simulation conditions are presented in Table 3. The transport parameters required for performing the simulations were obtained according to the referenced equations in Section 2.2 and can be found in Table 4. These values were determined at feed conditions. For the simulations presented in this work, a temperature of 298 K was used and a pressure profile inside the columns of the SMB component of the unit between 1.52 and 2.15 bar, with a feed composition, y_F, of 50% methane and 50% nitrogen. Also, cyclic steady state was considered achieved when the product purities remained constant between consecutive cycles, while ensuring mass conservation for both components. This way, cyclic steady state was reached in approximately 35 cycles. Fig. 2 shows the separation region obtained for this set of operating conditions, from which the optimal flow rate conditions in each section can be determined (full black line). The procedure employed to determine the boundaries of the region is analogous to that described for the SMB process in the referenced work [15]. Briefly, for a given switching time, a low value of feed flow rate, Q_F, is first selected and different values of displacement flow rate, Q_{Disp}, are screened until the product specifications are met. Once the limits are identified for that feed flow rate, its value is increased and the procedure is repeated for progressively higher values until the complete separation region is defined.

Also, in addition to the purity specifications (97% for the methane-rich stream and 99% for the nitrogen-rich stream), two restrictions for the productivity were also considered to ensure positive values for both products. To derive the equations that define the boundaries of separation region in terms of productivity, a range of Q_{II} and Q_{III} pairs was scanned, and the performance parameters were evaluated. These restrictions can also be found in Fig. 2.

Based on the analysis of Fig. 2, to prevent negative productivity values in the heavy component stream, the amount of methane used to displace the adsorbed phase in zone II during a step cannot exceed the amount of methane produced during the blowdown sub-step. This is translated by Eq. (65) and defines the yellow vertical dashed line in Fig. 2.

Additionally, negative methane productivities are also obtained if the amount of methane removed at the column outlet during the purge sub-step exceeds the amount of methane fed to the system, as methane losses occur mainly during the purge sub-step. By the definition of methane recovery, Eq. (66) can be defined, which describes the yellow slanted dotted line in Fig. 2.

This way, the following constraints can be established:

$$F_{Disp}\, t^* < \Delta n_{blow,CH_4}, \quad \Delta n_{blow,CH_4} = \frac{\Delta P_{blow}\, \varepsilon_t\, V}{R_g T_{blow}} + \Delta q_{blow,CH_4}\, m \tag{65}$$

$$F_F\, y_{F,CH_4}\, t^* > n_{pg,out,CH_4} \tag{66}$$

where $\Delta n_{blow,CH_4}$ is the amount of methane produced during the blowdown sub-step, ΔP_{blow} is the pressure difference between the start and end of the blowdown sub-step, ε_t is the total porosity, $\Delta q_{blow,CH_4}$ is the adsorbed concentration change observed during the blowdown sub-step, m is the adsorbent mass, and n_{pg,out,CH_4} is the amount of methane exiting the column during the purge sub-step.

To estimate n_{pg,out,CH_4}, the total moles of CH_4 remaining in the column after the blowdown sub-step are calculated. This estimation accounts for the CH_4 present in both the bed and particle voids, as well as the adsorbed phase, all evaluated at P_{low}.

To prevent negative productivities for the nitrogen stream, a feed flow rate restriction can be found:

Table 5
Fitting parameters for the Langmuir isotherm for the calculation of the $Q_{F,max}$.

Species	$q_{m,i}$ / mol·m^{-3}	$b_{0,i} \times 10^6$ / m^3 mol^{-1}	$-\Delta H_i$ / J·mol^{-1}
CH_4, ***A***	2201.2	7.10	17,232.4
N_2, ***B***	3783.9	8.91	11,959.9

$$F_F\, y_{F,N_2}\, t^* > F_{pg,in,N_2}\, t_{pg} \tag{67}$$

where F_{pg,in,N_2} is the purge molar flow rate of nitrogen, which is an approximation to the nitrogen purged during the purge sub-step, F_{pg,out,N_2}. This equation defines the teal slanted dash-dot line in Fig. 2.

In addition to the productivity restrictions presented above, another feed limitation can be found through the equilibrium theory. As such, the maximum feed flow rate limit, also presented in Fig. 2 (dash-double-dot line), was estimated based on the equilibrium theory for non-linear and diluted systems described by a Langmuir isotherm as proposed by Mazzotti *et al* [35]. Thus, to calculate this value, the N_2 and CH_4 adsorption equilibrium data previously available [15] was refitted with the Langmuir model to ensure compatibility with the equilibrium theory equations (Eq. (68) to (69)). The obtained parameters are presented in Table 5.where $q_{m,i}$ is the saturation capacity of component i, $b_{0,i}$ is the adsorption affinity constant at infinite temperature of component i and ΔH_i is the enthalpic parameter of component i for the Langmuir model. With these values, the maximum feed flow rate, $Q_{F,max}$, was estimated by solving the equation presented below:

$$Q_{F,max} = \left(\frac{\omega_G[\omega_F(\lambda_A - \lambda_B) + \lambda_B(\lambda_B - \omega_F)]}{\lambda_B(\lambda_A - \omega_F)} - \frac{\lambda_B \omega_G}{\lambda_A} \right) \cdot \frac{(1-\varepsilon)LA}{t^*}, \; \lambda_i = q_{m,i} b_i \tag{68}$$

With the temperature-dependent adsorption affinity constant of component i, b_i, being calculated using the Van't Hoff equation (Eq. (64)) and where λ_i is the adsorptivity of component i, and A is the cross-section area of the bed.

$\omega_G > \omega_F > 0$ are equilibrium theory parameters and are given by the roots of the quadratic equation:

$$\left(1 + b_A C_A^F + b_B C_B^F\right)\omega^2 - \left[\lambda_B\left(1 + b_A C_A^F\right) + \lambda_A\left(1 + b_B C_B^F\right)\right]\omega + \lambda_A \lambda_B = 0 \tag{69}$$

Where C_i^F is the feed concentration of each component.

The obtained value for $Q_{F,max}$, in $m^3 \cdot s^{-1}$, can then be converted to SLPM. However, this value can serve only as an approximation, as it neglects the mass transfer resistance effects and assumes a diluted system, whereas this process involves a non-diluted system where gas velocity variations occur. This way, a slight discrepancy is observed between the value calculated with the equilibrium theory and the actual $Q_{F,max}$, obtained at the upper boundary of the separation region, as introducing mass transfer resistances reduces the size of the feasible separation region.

After establishing the productivity constraints, the feasible separation region is determined based on the specified operating conditions and purity requirements. Defining these boundaries in advance reduces the computational effort involved in determining the optimal flow rate conditions, as they provide both the maximum displacement gas flow rate and the minimum viable feed flow rate for the process. These boundaries define the starting point for the search of the separation region.

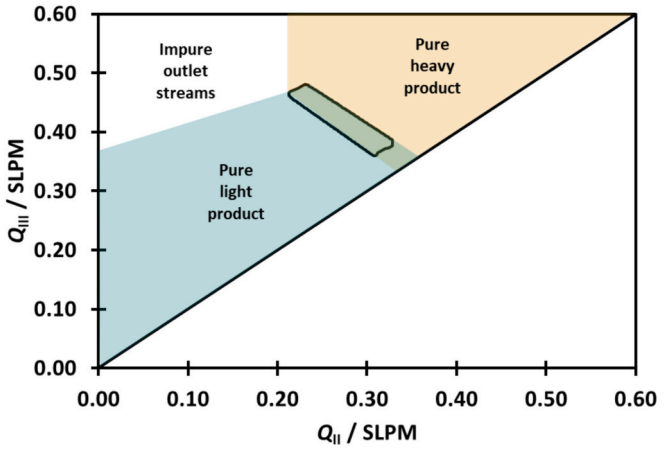

Fig. 3. Regions of the Q_{II}/Q_{III} plane in terms of purity of the outlet streams.

In Fig. 3, the different regions of the Q_{II}/Q_{III} plane regarding the purity of the outlet streams are defined. If a low displacement gas flow rate is used, then the nitrogen is not sufficiently displaced from the column, contaminating the methane stream produced during the blowdown sub-step above the 3% limit. On the other hand, if the flow rate in zone III is too high, then methane is carried with the fluid and the light product is contaminated. A combination of the two leads to impure heavy and light products.

Once the separation region is obtained, the concentration fronts inside the hybrid system were analysed to understand the multicomponent adsorption dynamics at cyclic steady state. For the columns in Zone II and III (SMB component of the hybrid unit), the internal molar composition profile at 10%, 50%, and 90% of the switching time was determined. For the column under PSA operation, the concentration profiles were obtained at the beginning and end of each sub-step, to account for the pressure changes imposed during the sequence. To do so, an operation point inside the separation region was selected, corresponding to a Q_{Disp} of 0.227 SLPM (with a composition equivalent to the average concentration of the heavy product) and a Q_F of 0.238 SLPM (Case 4, 50% CH_4/50% N_2). Fig. 4 and Fig. 5 show the obtained concentration profiles. Fig. 6 shows the pressure history, during a cycle, for column 8, where the first seven steps represent the pressure variation inside the columns in SMB operation (1.52–2.15 bar), while the last step corresponds to the regeneration step in section I, where the pressure inside the column is decreased to P_{low} (0.1 bar) during the blowdown sub-step, is equal to P_{low} during the purge sub-step and returns to P_{high} (1.52 bar) in the pressurization sub-step.

It can be noted, in Fig. 4, that the defined CH_4 displacement gas flow rate is sufficient to ensure that the first column becomes saturated with methane, preparing it for the PSA sequence in the next step. Additionally, in the adsorption zone, CH_4 is preferentially adsorbed on the solid phase. Due to the periodic column switching that simulates solid movement in the SMB operation, the CH_4 concentration front shifts downstream. In contrast, N_2, being less retained in the adsorbent, travels with the fluid phase leading to an increase in the N_2 molar fraction within these columns. During a step, the concentration fronts move in the direction of the fluid flow within the SMB component of the unit, from one column to another, until the switching occurs. The internal concentration profiles suggest that a higher flow rate in Zone III could be used, allowing an increase in the process feed flow rate, moving closer to the upper boundary of the defined separation region. To support this, the internal profile at 50% of the switching time, for the operation point located at the upper boundary of the separation region, is provided in Fig. S1.

Analysing Fig. 5, the heavy product gas is obtained by desorbing the full methane column from the displacement zone (corresponding to column I of Zone II, before the switch), during the blowdown sub-step. Also, the defined purge flow rate is enough to ensure that most of the methane is removed from the column. The pressurization step then increases the pressure back to the high pressure employed at the end of Section III.

As previously mentioned, in the SMB/PSA hybrid process, the heavy product is produced during the blowdown, while the light product gas corresponds to the outlet stream at the end of the adsorption zone (corresponding to column V of Zone III). In Fig. 7, the concentration histories for both product streams are presented. Fig. S2 provides the molar fraction histories for the heavy and light product streams.

The concentration histories (Fig. 7) and molar fraction histories (Fig. S2) show that high purity streams are obtained for both products, with an average molar fraction of 99% methane for the CH_4-rich stream and 99% nitrogen for the N_2-rich stream.

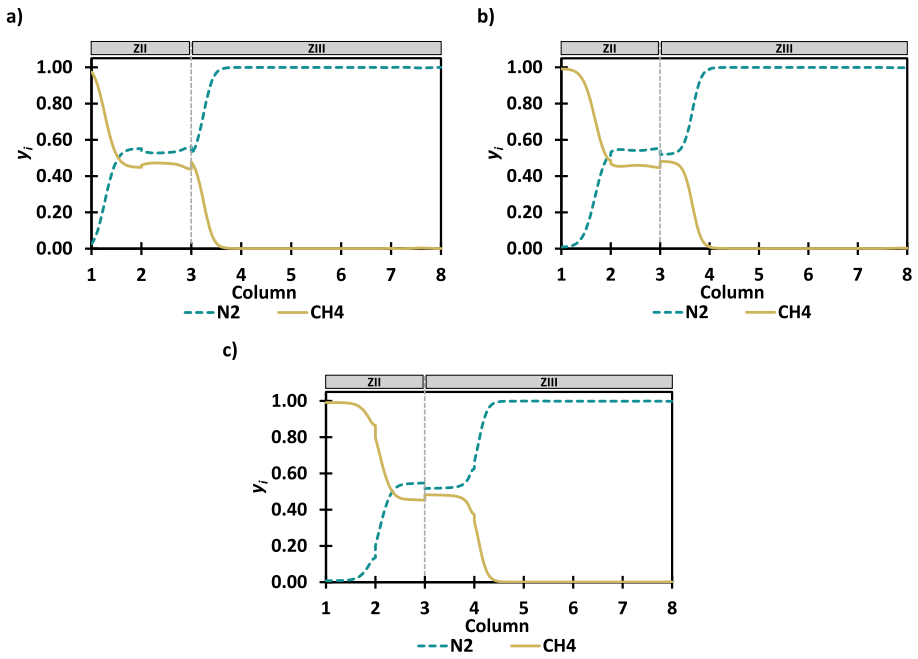

Fig. 4. Internal profiles at a) 10%, b) 50%, and c) 90% of the switching time for the columns in Zone II and III, operating in SMB mode, obtained at cyclic steady state at the defined operating conditions.

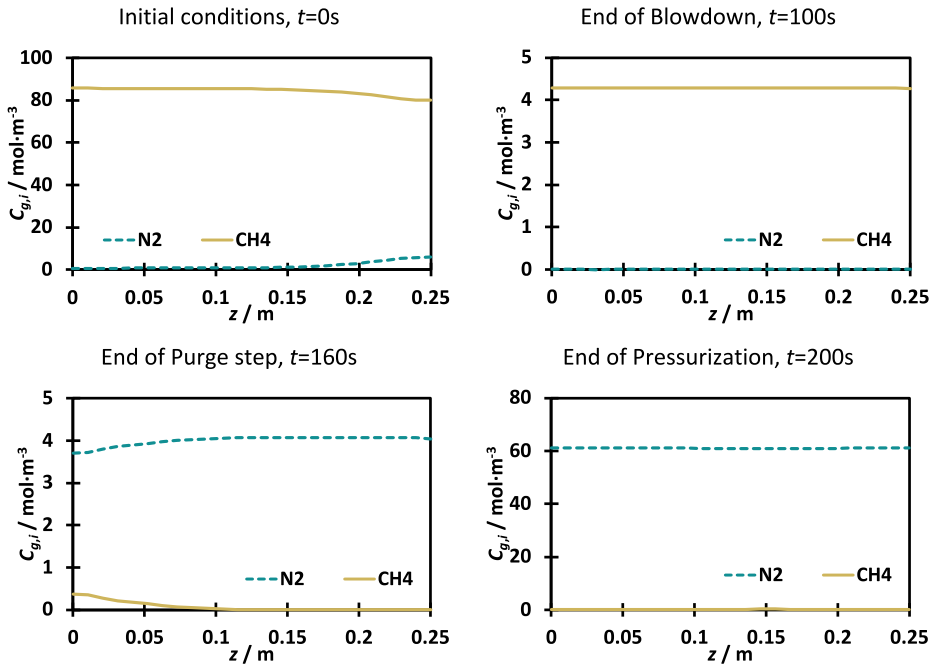

Fig. 5. Concentration profiles at the end of each sub-step of the PSA sequence, obtained at cyclic steady state.

3.1. Parametric study

A parametric study is essential for understanding how key operating variables affect the performance of the hybrid SMB/PSA process. Parameters such as switching time, duration of the PSA sub-steps, purge gas flow rate, feed composition and the pressure reached during the desorption steps (P_{low}) directly impact the separation region, purity, recovery, productivity and power consumption. By analysing these factors, it is possible to identify optimal operating conditions, improve the process efficiency, and expand the feasible separation region. This study provides insights into how each parameter affects the overall performance of the hybrid system. In each subsection, the operating conditions for each case are summarised in Table 6, Table 7, Table 9 and Table 11. For all cases, a temperature of 298 K was used and a pressure profile inside the columns of the SMB component of the unit between 1.52 and 2.15 bar, with a feed composition of 50% methane and 50% nitrogen. The performance parameters and power consumption values were calculated using Eq. (50) to Eq. (62) provided in Section 2.4.

3.1.1. Switching time

The effect of the switching time on the hybrid process was investigated. To do so, the separation regions were computed for two addi-

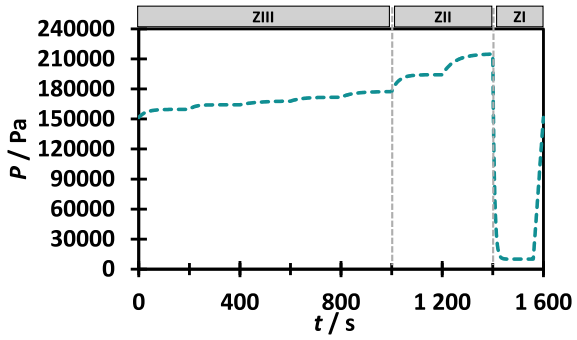

Fig. 6. Pressure history at the outlet of Column 8, during a cycle. The vertical lines indicate the transitions between sections as the column is assigned to Section III (first five steps), Section II (next two steps), and Section I (last step) during the cycle.

tional switching times, 100 s and 300 s, while maintaining the initial time percentage of the switching time for each of the sub-steps of the PSA sequence (50% for the blowdown, 30% for the purge, and 20% for the pressurization sub-step) and adjusting the purge flow rate accordingly. The operating conditions for each case are shown in Table 6. Case 1 refers to the initial set of operating conditions used for the determination of the separation region presented in Section 3. In Case 2 and Case 3, only the switching time and, consequently, the sub-step durations were altered. Once again, the values of Q_{Disp} and Q_F were varied to define the limits of the separation region.

The obtained separation regions are presented in Fig. 8. As observed, changing the switching time shifts the operating window, affecting the flow rate ratios in the different zones of the SMB component of the unit. This effect is also observed in conventional SMB processes, as changing the switching time of the process changes the equivalent solid velocity throughout the system ($u_s = L/t^*$) [18]. This way, increasing the switching time shifts the operating conditions toward lower flow rates in zones II and III, to avoid the more retained species, CH_4, from contaminating the light product stream in section III. On the contrary, reducing the switching time leads to higher flow rates in these zones to achieve complete separation of the feed mixture, ensuring that the less retained species does not move downward to section II and contaminate the heavy product stream. Also, a higher switching time results in a smaller separation region, which may hinder the feasibility of the separation. Reducing the switching time results in a larger separation region. However, it may lead to mass transfer limitations, which compromise the separation efficiency.

To verify the equivalence to the conventional SMB, for each separation region, the section flow rates were converted into the dimensionless ratio of the interstitial fluid and solid velocities, $\gamma_j = u_j/u_s$, and the γ_{II}/γ_{III} plots were compared. This comparison can be found in Fig. 9.

As observed, the separation regions overlap one another, indicating that the values of γ_j are the same regardless of the switching time. This is important from a design perspective, as with this equivalence, we can predict the operating flow rates when changing the switching time of the process.

3.1.2. PSA sub-step time and purge flow rate

To assess the impact of the duration of each sub-step of the PSA sequence, the percentage of the switching time allocated to each of the sub-steps (blowdown/purge/pressurization) was modified. In addition to Case 4 (50%/30%/20%), which corresponds to the operating conditions used for the analysis of the concentration fronts inside the hybrid unit in Section 3, two cases were examined: 25%/50%/25% (Case 5) and 10%/80%/10% (Case 6). The operating conditions used in each case are presented in Table 7. The methane purity, recovery, and productivity were obtained with and without the recovery of the methane during the purge sub-step, and the power consumption per kilogram of methane produced was determined. The simulation results are summarised in Table 8.

Table 6
Operating conditions defined for each case studied in the study of the effect of the switching time in the hybrid process.

Operating conditions	Case 1	Case 2	Case 3
P / bar	1.52–2.15	1.52–2.15	1.52–2.15
T / K	298	298	298
y_F	N_2: 0.5 CH_4: 0.5	N_2: 0.5 CH_4: 0.5	N_2: 0.5 CH_4: 0.5
P_{high} / bar	1.52	1.52	1.52
P_{low} / bar	0.10	0.10	0.10
t^* / s	200	100	300
t_{blow} / s	100	50	150
t_{pg} / s	60	30	90
t_{press} / s	40	20	60
Q_{pg} / SLPM	0.1	0.2	0.067

Table 7
Operating conditions defined for each case studied in the study of the influence of the sub-step duration and purge flow rate in the hybrid process performance.

Operating conditions	Case 4	Case 5	Case 6
P / bar	1.52–2.15	1.52–2.15	1.52–2.15
T / K	298	298	298
y_F	N_2: 0.5 CH_4: 0.5	N_2: 0.5 CH_4: 0.5	N_2: 0.5 CH_4: 0.5
P_{high} / bar	1.52	1.52	1.52
P_{low} / bar	0.1	0.1	0.1
t^* / s	200	200	200
t_{blow} / s	100	50	20
t_{pg} / s	60	100	160
t_{press} / s	40	50	20
Q_{disp} / SLPM	0.227	0.227	0.227
Q_F / SLPM	0.238	0.238	0.238
Q_{pg} / SLPM	0.1	0.1	0.1
$Q_{pg,\ min}$ / SLPM	0.06	0.035	0.022

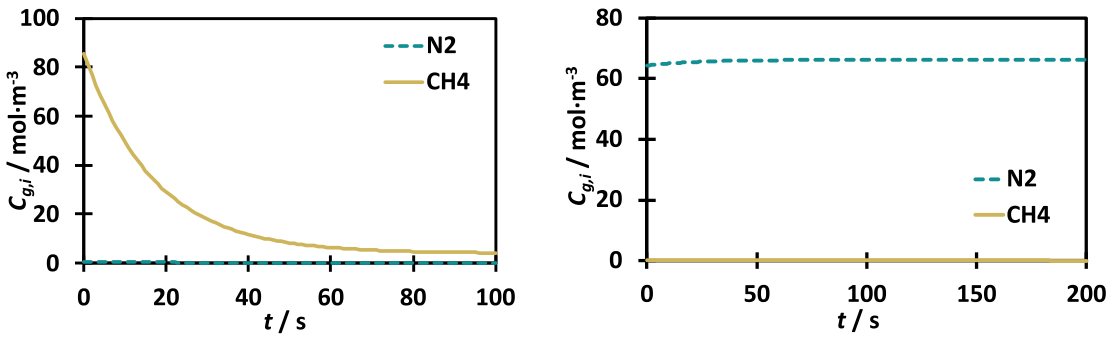

Fig. 7. Concentration histories obtained for the heavy product gas, CH_4 (left) and light product gas, N_2 (right).

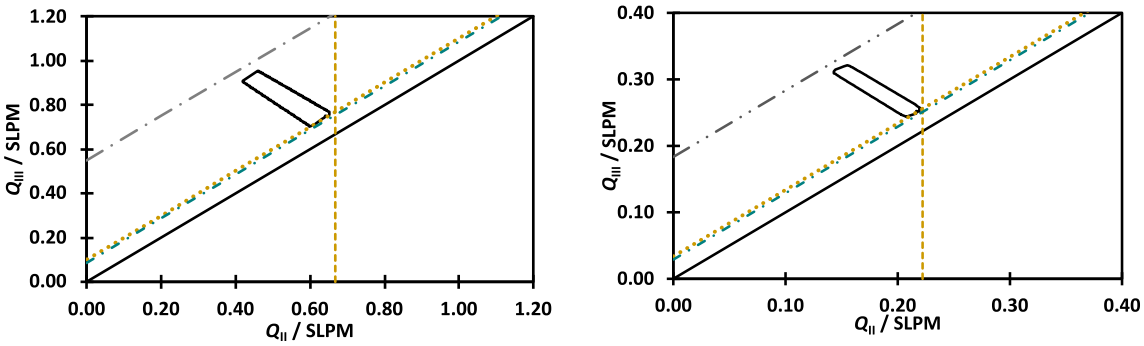

Fig. 8. Hybrid process separation region for an equimolar CH_4/N_2 mixture using BPL determined with the complete model, with a 1–2-5 column configuration, for a switching time of 100 s (left) and 300 s (right), and heavy and light component purities of 97 and 99%, respectively (full black line). The yellow lines represent the displacement gas (dashed line) and feed flow rate (dotted line) restrictions for positive CH_4 productivity. The teal line represents the feed flow rate restriction for positive N_2 productivity (dash-dot line). The slanted grey line represents the maximum feed flow rate constraint obtained through the equilibrium theory (dash-double-dot line).

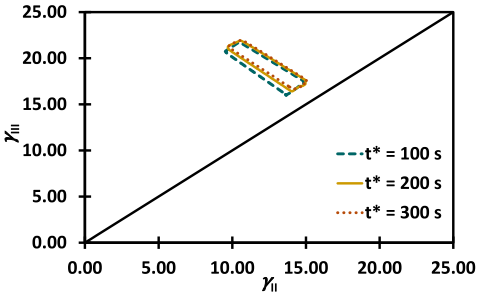

Fig. 9. Comparison of the separation regions computed for a switching time of 100, 200, and 300 s in terms of γ_j.

Table 8
Performance parameters obtained for each run performed with different sub-step times, at a purge flow rate of 0.1 SLPM and minimum purge flow rate.

	Case 4		Case 5		Case 6	
Q_{pg} / SLPM	0.1	0.06	0.1	0.035	0.1	0.022
Pu_{CH_4} / %	99.16	99.23	99.15	99.23	99.13	99.23
Pu_{N_2} / %	99.83	99.01	99.99	98.98	99.99	98.98
Rec_{CH_4} / %	76.29	76.62	75.87	76.27	72.94	73.41
Rec_{N_2} / %	81.12	90.71	64.46	91.19	39.28	91.26
Pu_{CH_4} with purge / %	96.98	97.01	96.97	96.98	97.05	97.00
Rec_{CH_4} with purge / %	96.22	97.15	95.91	97.32	94.97	97.27
$Prod_{CH_4}$ / kg·m$_{ads}^{-3}$·h^{-1}	9.0	9.0	8.9	9.0	8.6	8.7
$Prod_{N_2}$ / kg·m$_{ads}^{-3}$·h^{-1}	16.7	18.7	13.3	18.8	8.1	18.8
$Prod_{CH_4}$ with purge / kg·m$_{ads}^{-3}$·h^{-1}	11.3	11.5	11.3	11.5	11.2	11.5
Power consumption / W·h·kg$_{CH4}^{-1}$	503.0	476.0	555.7	491.3	648.3	525.8

Analysing the product stream purities confirms that the purity requirements were met for both components in all simulated cases. This was expected, since the selected operation point lies within the computed separation region.

In terms of recovery of each product, discarding the purge outlet stream leads to a low methane and nitrogen recovery, with recovery values below 76.3% and 81.1% for the heavy and light products, respectively. However, if a portion of the purge outlet stream is recovered as methane product (while the methane purity specification is kept above 97%), both recovery and productivity can be significantly improved, reaching up to 97.32% and 11.5 kg·m$_{ads}^{-3}$·h^{-1}, respectively, for the main product.

The results also show that the N_2 recovery is significantly impacted when increasing the duration of the purge sub-step, without minimising the purge flow rate. This results in excessive nitrogen consumption, halving the productivity of the light product for the longest purge sub-step.

To improve the recovery and productivity of the light component stream, the nitrogen purge flow rate was tuned for each case. To do so, the purge flow rate was decreased until the nitrogen stream purity was compromised, indicating that the desorption of the adsorbed methane in the purge sub-step was inefficient. The minimum Q_{pg} obtained for each case is presented in Table 8, as well as the performance parameters achieved for each run. The concentration histories during the PSA sequence for each run can be found in Fig. 10, Fig. 11, and Fig. 12.

By minimising the purge flow rate for each case, both nitrogen recovery and productivity values increased, reaching a maximum value of 91.26% and 18.8 kg·m$_{ads}^{-3}$·h^{-1} for the defined conditions. Also, if the purge flow rate is minimised to account for the increase in the duration of the purge sub-step, most of the methane that would be lost during the purge sub-step can be recovered. This way, the maximum methane recovery and productivity of 97.32% and 11.5 kg·m$_{ads}^{-3}$·h^{-1}, respectively, can be achieved for the tested flow rate conditions. The methane productivity (11.5 kg·m$_{ads}^{-3}$·h^{-1} or 1.07 mol·kg$_{ads}^{-1}$·h^{-1}) is comparable to the values reported in literature for adsorptive processes for methane upgrade of equimolar feed mixtures (0.61 mol·kg$_{ads}^{-1}$·h^{-1} [36], 0.93–1.07 mol·kg$_{ads}^{-1}$·h^{-1} [26], and 1.64 mol·kg$_{ads}^{-1}$·h^{-1} [28]).

Blowdown duration shows no significant influence on the steady-state performance parameters for the heavy component product stream (recovery and productivity). This is expected, as the process ensures that the column pressure reaches the target low pressure, P_{low}, during the blowdown interval. For the blowdown durations considered, the full mathematical model is employed, which accounts for the mass transfer resistances effects, and so, desorption is not assumed to be instantaneous. However, the kinetics are sufficiently fast that the desorption is equilibrium-controlled. As shown in Fig. 10 to Fig. 12, the bulk compositions during the blowdown step reach nearly constant values, indicating that gas–solid equilibrium is achieved within the specified blowdown time. Also, the faster concentration decrease observed at shorter blowdown durations is not caused by faster desorption kinetics, but rather by a faster pressure decrease. Thus, the total amount of gas released during this sub-step remains nearly constant, regardless of its duration.

A similar observation applies to the pressurization sub-step. Since the column pressure is always increased to the target high pressure, P_{high}, by the end of the pressurization time, t_{press}, the amount of gas utilised is effectively the same. Therefore, varying the duration of the pressurization sub-step does not influence the recovery and productivity of the light species.

In terms of power consumption, the blowdown sub-step contributes the most to the overall energy requirements. Reducing the blowdown

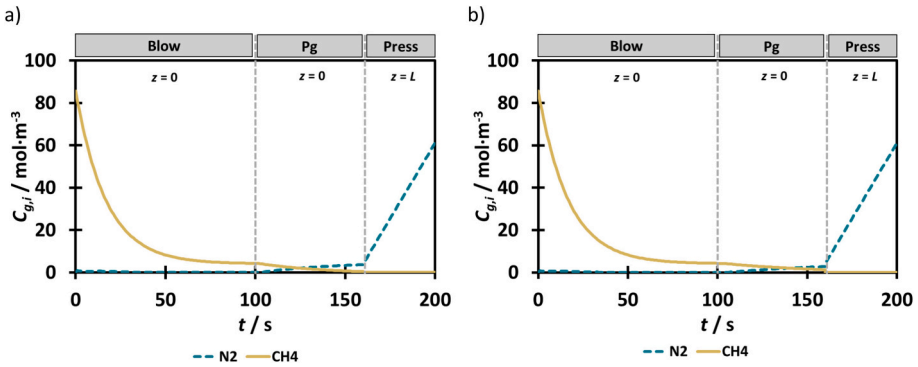

Fig. 10. Concentration histories during the PSA sequence for Case 4: a) with a purge flow rate of 0.1 SLPM, and b) with a purge flow rate of 0.06 SLPM.

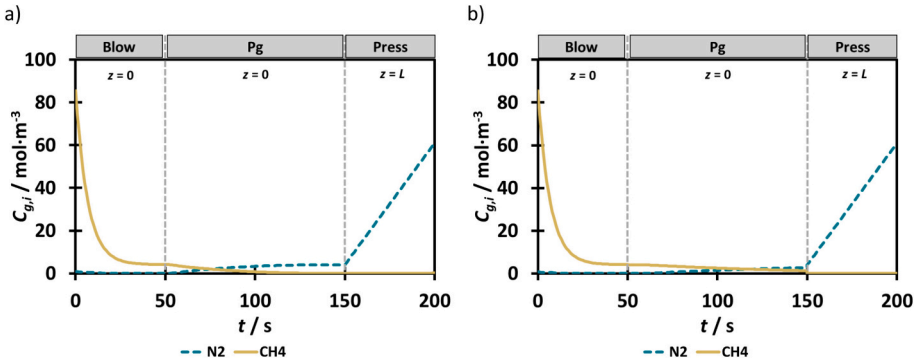

Fig. 11. Concentration histories during the PSA sequence for Case 5: a) with a purge flow rate of 0.1 SLPM, and b) with a purge flow rate of 0.035 SLPM.

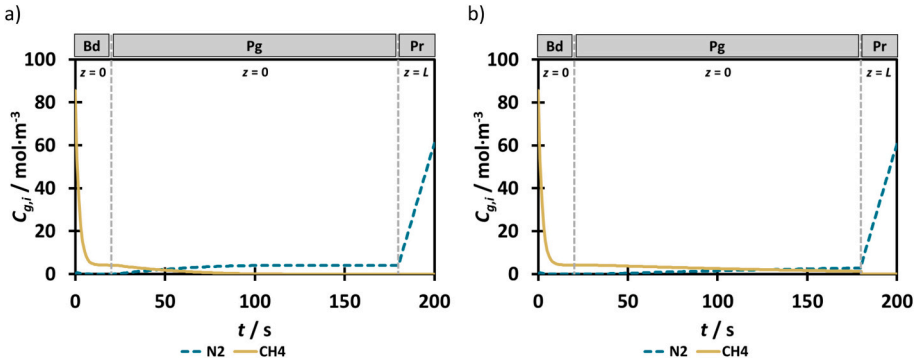

Fig. 12. Concentration histories during the PSA sequence for Case 6: a) with a purge flow rate of 0.1 SLPM, and b) with a purge flow rate of 0.022 SLPM.

duration increases power consumption by 3.1–6.6% to maintain the performance parameters achieved for the CH_4 stream. As such, for the shortest blowdown duration of 20 s, the power consumption reached 525.8 W·h·kg$^{-1}_{CH4}$. Nevertheless, the power consumption values across the three examined cases remained within the same order of magnitude, with the lowest value being 476.0 W·h·kg$^{-1}_{CH4}$ (approximately 1.7 MJ per kilogram of methane produced). These values are comparable to the ones reported in literature for other PSA-type processes for methane purification: 1.4 MJ·kg$^{-1}_{CH4}$ (feed N_2 content of 25%) [37], 4 MJ·kg$^{-1}_{CH4}$ (feed N_2 content of 50%) [36], 1.6–2.4 MJ·kg$^{-1}_{CH4}$ (feed N_2 content of 12%) [38]. A sensitivity analysis showed that increasing the vacuum pump efficiency from 60% to 80% would reduce the specific energy consumption by approximately 21%.

This way, the percentage of the switching time allocated to each of the PSA sub-steps does not seem to have an impact on the efficiency of the process, as long as the purge flow rate is minimised according to the duration of the purge sub-step. Also, part of the purge outlet stream can be recovered to not waste the non-desorbed methane that remains inside the column after the blowdown sub-step occurs, maximising the methane recovery. To further improve the recovery and productivity of both product streams, future process designs may also consider recycling the purge outlet stream to the feed inlet.

3.1.3. *Feed composition*

The effect of feed composition was investigated to assess process performance under both more challenging and more favourable separation conditions. The feed composition was varied from the base case of 50% CH_4/50% N_2 to 20% CH_4/80% N_2 and 80% CH_4/20% N_2, while the remaining operating conditions presented in Table 3 (Case 1) were kept constant. For each composition, the feasible separation region was determined using the same procedure described in Section 3, as presented in Fig. 13.

The effect of feed composition on the separation performance can be clearly observed from the shape and position of the computed separation

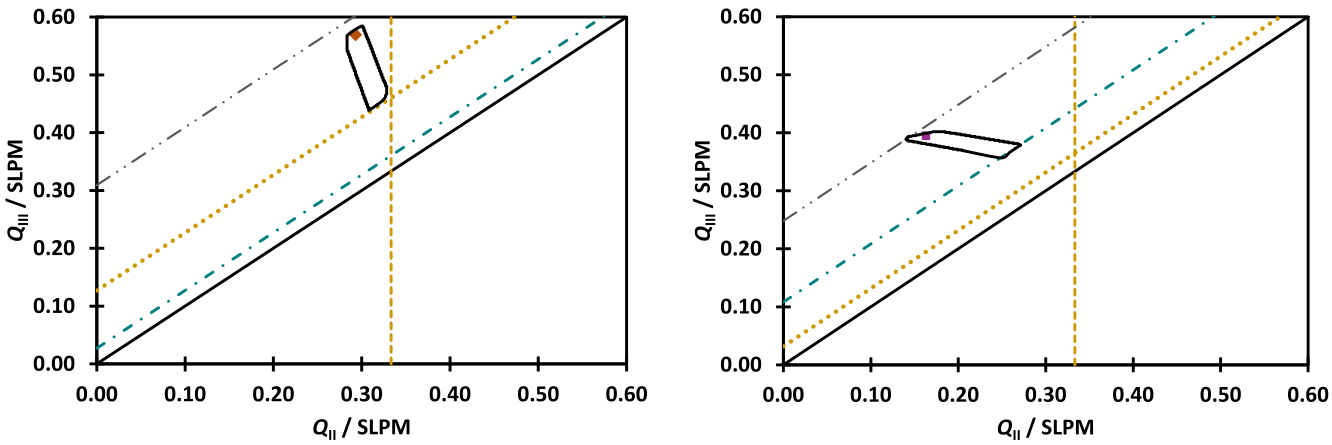

Fig. 13. Hybrid process separation region for an equimolar CH_4/N_2 mixture using BPL determined with the complete model, with a 1–2-5 column configuration, for a feed composition of 20% CH_4/ 80% N_2 (left) and 80% CH_4/ 20% N_2 (right), and heavy and light component purities of 97 and 99%, respectively (full black line). The yellow lines represent the displacement gas (dashed line) and feed flow rate (dotted line) restrictions for positive CH_4 productivity. The teal line represents the feed flow rate restriction for positive N_2 productivity (dash-dot line). The slanted grey line represents the maximum feed flow rate constraint obtained through the equilibrium theory (dash-double-dot line). The points (◆) and (■) represents the operating conditions for Case 7 and Case 8, respectively.

Table 9
Operating conditions defined for each case studied in the study of the influence of the feed composition in the hybrid process performance.

Operating conditions	Case 4	Case 7	Case 8
P / bar	1.52–2.15	1.52–2.15	1.52–2.15
T / K	298	298	298
y_F	N_2: 0.5 CH_4: 0.5	N_2: 0.8 CH_4: 0.2	N_2: 0.2 CH_4: 0.8
P_{high} / bar	1.52	1.52	1.52
P_{low} / bar	0.1	0.1	0.1
t^* / s	200	200	200
t_{blow} / s	100	100	100
t_{pg} / s	60	60	60
t_{press} / s	40	40	40
Q_{disp} / SLPM	0.227	0.293	0.163
Q_F / SLPM	0.238	0.272	0.232
Q_{pg} / SLPM	0.06	0.058	0.062

Table 10
Performance parameters obtained for each run performed with different feed compositions.

	Case 4	Case 7	Case 8
Pu_{CH_4} / %	99.23	99.52	98.93
Pu_{N_2} / %	99.01	98.98	99.01
Rec_{CH_4} / %	76.62	47.60	84.93
Rec_{N_2} / %	90.71	95.45	73.34
Pu_{CH_4} with purge / %	97.01	96.97	96.97
Rec_{CH_4} with purge / %	97.15	93.21	97.82
$Prod_{CH_4}$ / $kg \cdot m_{ads}^{-3} \cdot h^{-1}$	9.0	2.6	15.5
$Prod_{N_2}$ / $kg \cdot m_{ads}^{-3} \cdot h^{-1}$	18.7	35.9	5.9
$Prod_{CH_4}$ with purge / $kg \cdot m_{ads}^{-3} \cdot h^{-1}$	11.5	5.0	17.9
Power consumption / $W \cdot h \cdot kg_{CH4}^{-1}$	476.0	1596.4	420.7

regions. As the CH_4 content in the feed increases, the separation region becomes less sharply defined, and its upper boundary shifts downward and toward lower displacement flow rates. This behaviour is expected, since a lower N_2 content in the feed reduces the amount of CH_4 displacement gas required to displace the nitrogen in Section II.

The productivity constraints defined by Eqs. (65) to (67) remain applicable for all feed compositions. However, the constraint that actively limits the separation region changes as the N_2 content decreases. When N_2 is present at lower concentrations, the feed flow rate must remain sufficiently high to ensure positive N_2 productivity, as it must exceed the amount that is removed during the purge sub-step. As a result, the separation region becomes bounded by the N_2 productivity constraint rather than by CH_4 recovery limitation. If the productivity constraints were not active, the intersection of the separation region with the diagonal would remain unchanged, as it corresponds to the infinite dilution conditions of the system. The effects of the feed composition observed for the hybrid process are consistent with those reported for conventional SMB systems operating with non-linear adsorption isotherms, as discussed by Mazzotti *et al* [39].

Afterward, an operating point within each region was selected, corresponding to Case 7 and Case 8. In all cases, the purge flow rate was minimised. The corresponding operating conditions and simulation results are reported in Table 9 and Table 10, respectively.

The results show that the hybrid SMB/PSA process can effectively upgrade feed streams containing 20%, 50%, and 80% CH_4 to a product purity of 97%, with methane recoveries exceeding 93%. For feeds with low CH_4 content, lower productivity (5.0 $kg \cdot m_{ads}^{-3} \cdot h^{-1}$ or 0.46 $mol \cdot kg_{ads}^{-1} \cdot h^{-1}$) and higher energy consumption (approximately 5.8 $MJ \cdot kg_{CH4}^{-1}$) are observed, as a result of the reduced methane concentration in the feed stream. Nevertheless, the productivity value remains comparable to those reported for other adsorption-based processes in the literature, such as 0.48 $mol \cdot kg_{ads}^{-1} \cdot h^{-1}$ for a 25% CH_4 feed [37], 0.99 $mol \cdot kg_{ads}^{-1} \cdot h^{-1}$ for a 20% CH_4 feed [40], and 0.52–0.6 $mol \cdot kg_{ads}^{-1} \cdot h^{-1}$ for a 30% CH_4 feed [26].

For mixtures with lower nitrogen content, the process performance improves significantly, yielding a higher methane throughput and reduced energy consumption compared to the base case (1.66

Table 11
Operating conditions defined for each case in the study investigating the effect of P_{low} on the performance of the hybrid process.

Operating conditions	Case 4	Case 9	Case 10
P / bar	1.52–2.15	1.52–2.15	1.52–2.15
T / K	298	298	298
y_F	N_2: 0.5 CH_4: 0.5	N_2: 0.5 CH_4: 0.5	N_2: 0.5 CH_4: 0.5
P_{high} / bar	1.52	1.52	1.52
P_{low} / bar	0.10	0.20	0.30
t^* / s	200	200	200
t_{blow} / s	100	100	100
t_{pg} / s	60	60	60
t_{press} / s	40	40	40
Q_{disp} / SLPM	0.227	0.227	0.227
Q_F / SLPM	0.238	0.238	0.238
Q_{pg} / SLPM	0.10	0.20	0.30

Table 12
Influence of the value of P_{low} in the performance parameters of the hybrid process.

	Case 4	Case 9	Case 10
Pu_{CH_4} / %	99.16	99.10	99.04
Pu_{N_2} / %	99.83	99.73	99.65
Rec_{CH_4} / %	76.29	56.98	37.61
Rec_{N_2} / %	81.12	63.11	45.11
Pu_{CH_4} with purge / %	96.98	97.07	97.07
Rec_{CH_4} with purge / %	96.22	86.04	74.32
$Prod_{CH_4}$ / mol·m$_{ads}^{-3}$·h^{-1}	9.0	6.7	4.4
$Prod_{N_2}$ / mol·m$_{ads}^{-3}$·h^{-1}	16.7	13.0	9.3
$Prod_{CH_4}$ with purge / mol·m$_{ads}^{-3}$·h^{-1}	11.3	10.1	8.8
Power consumption / W·h·kg$_{CH4}^{-1}$	503.0	482.0	452.1

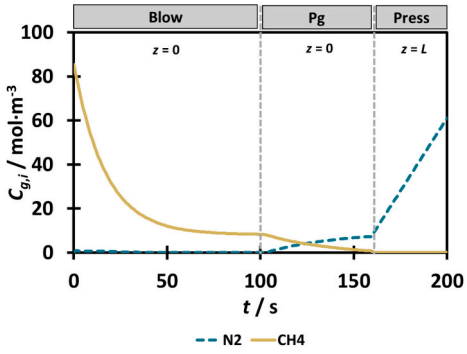

Fig. 14. Concentration history during the PSA sequence for Case 9, with a desorption pressure of 0.2 bar.

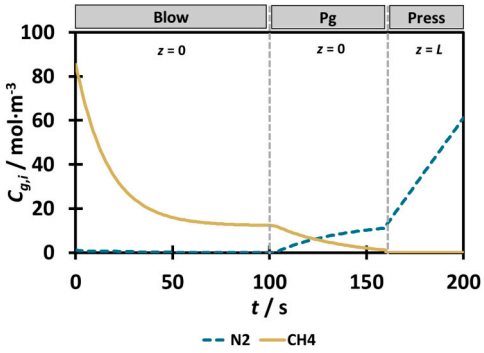

Fig. 15. Concentration history during the PSA sequence for Case 10, with a desorption pressure of 0.3 bar.

mol·kg$_{ads}^{-1}$·h^{-1} and 1.5 MJ·kg$_{CH4}^{-1}$, respectively). These values are similar to those reported for a DR-PSA process using an ETS-4 adsorbent by Wang et al., who achieved a productivity of 1.52 mol·kg$_{ads}^{-1}$·h^{-1} and energy consumption of 1.5 MJ·kg$_{CH4}^{-1}$ (85% CH_4 feed) [41]. In this case, a lower N_2 recovery is obtained due to the reduced nitrogen content in the feed stream, while a similar nitrogen purge is still required to displace the methane during the purge sub-step. This limitation can potentially be mitigated by recycling the purge outlet stream to the feed inlet, as suggested in the previous section.

3.1.4. Low pressure

The low pressure defined during the desorption steps in the PSA sequence greatly affects the overall power consumption, particularly due to the multiple vacuum stages required to reduce the pressure down to 0.1 bar. If a desorption pressure above 0.2 bar can be employed without compromising the process performance, energy efficiency can be improved. To test this possibility, two different values of P_{low} were tested – 0.2 (Case 9) and 0.3 bar (Case 10) - and their impact on the performance parameters was assessed. The purge flow rate was increased to compensate for the increase in the value of P_{low}. The operating conditions for each case are presented in Table 11. The corresponding results are summarised in Table 12. The concentration histories inside the column operating under PSA is presented in Fig. 14 and Fig. 15 for Case 9 and Case 10, respectively.

As observed, increasing the value of P_{low} results in incomplete desorption of methane, which negatively impacts the methane recovery. Also, to compensate for the poor methane desorption during the blowdown sub-step, a higher purge flow rate is required to ensure that the purity requirement for the nitrogen stream is met, leading to reduced process efficiency. As expected, the use of a very low pressure (0.10 bar) for regeneration has a high negative impact on the energy consumption. Although higher desorption pressures improve energy efficiency, this comes at the expense of overall process performance.

This indicates that, to optimize the CH_4/N_2 separation by an SMB/PSA hybrid process, the value of P_{low} needs to be set to very low values to ensure effective methane desorption and maximize product recovery and productivity.

4. Conclusions

In this work, an SMB/PSA hybrid process for the separation of CH_4/N_2 mixtures was implemented, and the influence of key parameters was assessed. This novel technique was able to produce high purity methane and nitrogen streams, meeting the 97% and 99% purity requirements specified for each component. By partially recovering the purge outlet stream as heavy product gas, the methane recovery and productivity can be increased up to 97.3% and 11.5 kg·m$_{ads}^{-3}$·h^{-1}, respectively. Optimising the purge flow rate utilised during this sub-step allows the recovery of the light product to be kept above 90%.

Also, increasing the value of P_{low} is inefficient in terms of process performance, as it reflects in a lower recovery of methane and, consequently, lower productivity. This way, to obtain a high purity and high recovery methane stream, the pressure during the desorption sub-steps in the PSA sequence needs to be set to very low values (0.1 bar), leading to a power consumption of 503.0 W·h·kg$_{CH4}^{-1}$.

A strategy was developed to determine the separation region of the hybrid SMB/PSA process, enabling a more efficient selection of the flow rate conditions when designing the separation cycles.

The presented results show that this advanced hybrid process can be a competitive alternative to the state-of-the-art nitrogen removal technologies for small-scale applications, allowing the production of purified methane with high throughputs. From an engineering perspective, implementation of the hybrid SMB/PSA process mainly involves managing process control aspects, including synchronized valve switching, step sequencing, and pressure modulation for adsorbent regeneration. When scaling-up, practical considerations related to pressure control, flow distribution, and equipment sizing need to be addressed as well.

Future work will focus on adapting the existing gas-SMB pilot unit to hybrid SMB/PSA operation, experimentally validating the process, and conducting multivariable optimization and techno-economic analysis for industrial applications.

Nomenclature

List of symbols

A	cross-section area of the column	m^2
a_p	particle/monolith channel specific area	m^{-1}
$b_{0,i}$	adsorption affinity constant at infinite temperature	bar^{-1}
b_i	temperature-dependent adsorption affinity constant of component i	bar^{-1}
C_i^F	feed concentration of component i	mol·m^{-3}
$C_{g,i}$	fluid phase concentration of component i	mol·m^{-3}

(*continued on next page*)

(*continued*)

$C_{g,T}$	total concentration in the fluid phase	$mol \cdot m^{-3}$
$C_{inlet,i}$	total inlet gas phase concentration of component i	$mol \cdot m^{-3}$
$C_{inlet,T}$	total inlet gas phase concentration	$mol \cdot m^{-3}$
c_P	gas mixture molar heat capacity at constant pressure	$J \cdot mol^{-1} \cdot K^{-1}$
$\overline{C_{p,i}}$	averaged mole concentration of component i inside the particle	$mol \cdot m^{-3}$
$\widehat{c}_{Ps}$	solid specific heat	$J \cdot kg^{-1} \cdot K^{-1}$
$\widehat{c}_{Pw}$	column wall specific heat	$J \cdot kg^{-1} \cdot K^{-1}$
$C_{s,i}$	concentration at the solid interface of component i	$mol \cdot m^{-3}$
c_V	gas mixture molar heat capacity at constant volume	$J \cdot mol^{-1} \cdot K^{-1}$
$c_{V,i}$	molar heat capacity of component i at constant volume	$J \cdot mol^{-1} \cdot K^{-1}$
D_{ax}	axial dispersion coefficient	$m^2 \cdot s^{-1}$
d_p	particle diameter	m
d_w	internal column diameter	m
e	width of the column wall	m
F	molar flow rate	$mol \cdot s^{-1}$
F_{disp}	displacement gas molar flow rate	$mol \cdot s^{-1}$
F_j	molar flow rate in each zone j	$mol \cdot s^{-1}$
h_f	film heat transfer coefficient between the gas phase and the solid / monolith wall	$W \cdot m^{-2} \cdot K^{-1}$
h_w	film heat transfer coefficient between the gas phase / monolith wall and the column wall	$W \cdot m^{-2} \cdot K^{-1}$
k_f	film mass transfer coefficient	$m \cdot s^{-1}$
k_{macro}	mass transfer resistance coefficient at the macropore level	s^{-1}
k_{micro}	mass transfer resistance coefficient at the micropore level	s^{-1}
L	column length	m
m	adsorbent mass	kg
M	molecular weight	$kg \cdot mol^{-1}$
$n_{pg,out,i}$	amount of i exiting the column during the purge sub-step	mol
NC	number of components	
N_{sites}	number of sites	
P	total pressure of the system	Pa or bar
P_{atm}	atmospheric pressure	Pa
P_i	partial pressure of component i	bar
P_{high}	pressure at the end of Section III	Pa
P_{inlet}	inlet pressure	Pa
P_{low}	low pressure during the desorption sub-steps	Pa
$Prod$	productivity	$kg_{A,B} \cdot m_{ads}^{-3} \cdot h^{-1}$
P_{outlet}	outlet pressure	Pa
Pu	purity	%
Q	flow rate	$m^3 \cdot s^{-1}$
Q_j	flow rate in each section	SLPM
Q_{disp}	displacement gas flow rate	SLPM
$Q_{F,max}$	maximum feed flow rate in the hybrid process	SLPM
q_i	adsorbed concentration of component i	$mol \cdot kg^{-1}$
q_i^*	adsorbed concentration of component i in equilibrium with $\overline{C_{p,i}}$	$mol \cdot kg^{-1}$
$\overline{q_i}$	particle averaged adsorbed concentration of component i	$mol \cdot kg^{-1}$
$q_{m,i}$	saturation capacity of component i	$mol \cdot kg^{-1}$
Q_{pg}	purge flow rate	SLPM
$Q_{pg,min}$	minimum purge flow rate	SLPM
Rec	recovery	%
R_g	ideal gas constant (=8.314)	$J \cdot mol^{-1} \cdot K^{-1}$
t	time	s
T	temperature of the system	K
t_{blow}	blowdown sub-step duration	s
T_{blow}	blowdown temperature	K
T_{inlet}	inlet temperature	K
$t_{int,pg}$	fraction of purge sub-step duration that is recovered	s
t^*	switching time	s
T_g	temperature of the gas phase	K
t_{pg}	purge sub-step duration	s
t_{press}	pressurization sub-step duration	s
T_s	temperature of the solid phase	K
T_w	temperature of the wall of the column	K
T_∞	the temperature of the surroundings	K
U	overall heat transfer coefficient	$W \cdot m^{-2} \cdot K^{-1}$
u_j	interstitial gas velocity in section j	$m \cdot s^{-1}$
u_0	superficial gas velocity	$m \cdot s^{-1}$
$u_{0,inlet}$	inlet superficial gas velocity	$m \cdot s^{-1}$
u_s	interstitial solid velocity	$m \cdot s^{-1}$
V	column volumn	m^3
ν_j	interstitial fluid velocity in section j	$m \cdot s^{-1}$

(*continued on next column*)

(*continued*)

W_{blow}	power consumption resultant from the vacuum pump during the blowdown sub-step in the hybrid process	W
W_{disp}	power consumption resultant from the compression of the displacement gas in the hybrid process	W
W_{pg}	power consumption resultant from the vacuum pump during the purge sub-step in the hybrid process	W
W_T	total power consumption	W
y_F	feed composition	
y_i	molar fraction in the gas phase of pure component i	
$\bar{y}$	average molar fraction	
z	axial direction	m

Greek letters

α_w	ratio of the internal surface area to the volume of the column wall	m^{-1}
α_{wl}	ratio of the logarithmic mean surface area of the column shell to the volume of the column wall	m^{-1}
γ	ratio between the heat capacity of the gas mixture at constant pressure and the heat capacity of the gas mixture at constant volume	
γ_j	dimensionless ratio of the interstitial fluid and solid velocities in section j	
$\Delta H_{i,k}$	enthalpic parameter of component i for site k	$J \cdot mol^{-1}$
$\Delta n_{blow,CH_4}$	amount of methane produced during the blowdown sub-step	mol
ΔP_{blow}	pressure difference between the start and end of the blowdown sub-step	Pa
$\Delta q_{blow,CH_4}$	adsorbed concentration change observed during the blowdown sub-step	$mol \cdot kg^{-1}$
ε	bed porosity	
ε_p	Particle/monolith wall porosity	
ε_t	total porosity	
η	compressor/vacuum pump efficiency	
λ	heat axial dispersion coefficient	$W \cdot m^{-1} \cdot K^{-1}$
λ_i	adsorptivity, $\lambda_i = q_{m,i} b_i$	
μ	gas mixture viscosity	Pa·s
ρ	gas mixture density	$kg \cdot m^{-3}$
ρ_b	bulk density	$kg \cdot m^{-3}$
ρ_p	particle/monolith wall apparent density	$kg \cdot m^{-3}$
ρ_w	column wall density	$kg \cdot m^{-3}$
ω_F, ω_G	equilibrium theory parameter defined as solution of Eq. (68)	

Subscripts and superscripts

i	component of the mixture
j	Section number
k	Number of columns
I, II, III	Section I, II, and III, respectively
F	Feed
A, B	Heavy and light component

Abbreviations

AC	activated carbon
DAEBDF	differential-algebraic equation - backward differentiation formulae
Disp	displacement gas
LDF	linear driving force
MOF	metal organic framework
OCFEM	orthogonal collocation on finite elements method
Pg	purge
Press	pressurization
PSA	pressure swing adsorption
SMB	simulated moving bed
VPSA	vacuum pressure swing adsorption

CRediT authorship contribution statement

Rafael O.M. Dias: Writing – review & editing, Writing – original draft, Validation, Software, Investigation, Data curation. **Alexandre F. P. Ferreira:** Writing – review & editing, Supervision, Funding

acquisition. **Alírio E. Rodrigues:** Writing – review & editing, Supervision, Funding acquisition. **Ana M. Ribeiro:** Writing – review & editing, Validation, Supervision, Methodology, Funding acquisition, Conceptualization.

Declaration of competing interest

The authors declare that they have no known competing financial interests or personal relationships that could have appeared to influence the work reported in this paper.

Acknowledgments

This work was financially supported by Fundação para a Ciência e a Tecnologia, I.P. /MCTES through national funds: LSRE-LCM, UID/50020/2025 (DOI: 10.54499/UID/50020/2025); and ALiCE, LA/P/0045/2020 (DOI: 10.54499/LA/P/0045/2020). Rafael Dias acknowledges his Ph.D. scholarship 2020.05095.BD, funded by FEDER funds through NORTE 2020 and by national funds through FCT/MCTES (DOI: 10.54499/2020.05095.BD). This paper is a result of the project "ECO-MOBES - Smart Mobility & Technologies for Resource Efficiency", with operation code at the Funds Platform (Balcão dos Fundos), NORTE2030-FEDER-02699500, co-financed by the European Union through the NORTE 2030 Regional Program, of Portugal 2030.

Appendix A. Supplementary data

Supplementary data to this article can be found online at https://doi.org/10.1016/j.cej.2026.175211.

Data availability

Data will be made available on request.

References

[1] J.G. Speight, Natural Gas: A Basic Handbook, Gulf Professional Publishing, 2018.
[2] K.S. Knaebel, H.E. Reinhold, Landfill gas: from rubbish to resource, Adsorpt 9 (1) (2003) 87–94, https://doi.org/10.1023/A:1023871415711.
[3] C. Windmeier, R.F. Barron, Cryogenic technology, Ullmann's encyclopedia of industrial, Chemistry (2013) 1–71.
[4] F. Rao, Z. Lu, Y. Guo, Z. Liu, C. Fu, X. Xie, C. Liao, T. Qi, G. Hu, The separation of methane and nitrogen in natural gas processing: a review, Sep. Purif. Technol. 363 (2025) 132107, https://doi.org/10.1016/j.seppur.2025.132107.
[5] B. Majumdar, S.J. Bhadra, R.P. Marathe, S. Farooq, Adsorption and diffusion of methane and nitrogen in barium exchanged ETS-4, Ind. Eng. Chem. Res. 50 (5) (2011) 3021–3034, https://doi.org/10.1021/ie1014124.
[6] R.P. Marathe, K. Mantri, M.P. Srinivasan, S. Farooq, Effect of ion exchange and dehydration temperature on the adsorption and diffusion of gases in ETS-4, Ind. Eng. Chem. Res. 43 (17) (2004) 5281–5290, https://doi.org/10.1021/ie049818+.
[7] S.M. Kuznicki, V.A. Bell, S. Nair, H.W. Hillhouse, R.M. Jacubinas, C.M. Braunbarth, B.H. Toby, M. Tsapatsis, A titanosilicate molecular sieve with adjustable pores for size-selective adsorption of molecules, Nature 412 (6848) (2001) 720–724, https://doi.org/10.1038/35089052.
[8] S. Cavenati, C.A. Grande, A.E. Rodrigues, Separation of methane and nitrogen by adsorption on carbon molecular sieve, Sep. Sci. Technol. 40 (13) (2005) 2721–2743, https://doi.org/10.1080/01496390500287846.
[9] A.I. Fatehi, K.F. Loughlin, M.M. Hassan, Separation of methane—nitrogen mixtures by pressure swing adsorption using a carbon molecular sieve, Gas Sep. Purif. 9 (3) (1995) 199–204, https://doi.org/10.1016/0950-4214(95)98227-C.
[10] F. Brandani, P. Pullumbi, C. Monereau, Nitrogen rejection from landfill gas using pressure swing adsorption, Adsorpt 27 (4) (2021) 603–617, https://doi.org/10.1007/s10450-021-00304-0.
[11] N.S. Wilkins, K.N. Pai, A. Rajendran, Optimization of pressure-vacuum swing adsorption processes for nitrogen rejection from natural gas streams using a nitrogen selective metal organic framework, Can. J. Chem. Eng. 100 (9) (2022) 2374–2393, https://doi.org/10.1002/cjce.24469.
[12] F. Zheng, L. Chen, R. Chen, Z. Zhang, Q. Yang, Y. Yang, B. Su, Q. Ren, Z. Bao, A robust two–dimensional layered metal–organic framework for efficient separation of methane from nitrogen, Sep. Purif. Technol. 281 (2022) 119911, https://doi.org/10.1016/j.seppur.2021.119911.
[13] W.B. Dolan, K.F. Butwell, Selective removal of nitrogen from natural gas by pressure swing adsorption, in: BASF Catalysts LLC, 2000. Patent number: US6444012B1.
[14] P.D.S.F. Barcia, D.A.S. Silva, S.D.D.S.C. Monteiro, Multi-stage psa process to remove contaminant gases from raw methane streams, in: Sysadvance Sistemas De Engenharia SA, 2023. Patent Number: US11701612B2.
[15] R.O.M. Dias, A.F.P. Ferreira, A.E. Rodrigues, A.M. Ribeiro, Gas-phase simulated moving bed for methane/nitrogen separation using a commercial activated carbon, Ind. Eng. Chem. Res. (2022), https://doi.org/10.1021/acs.iecr.2c01436.
[16] R.O.M. Dias, M.J. Regufe, A.A. Pereira, A.F.P. Ferreira, A.E. Rodrigues, A. M. Ribeiro, Methane upgrading on pelletised Maxsorb activated carbon by gas-phase simulated moving bed, Adsorpt 31 (1) (2024) 7, https://doi.org/10.1007/s10450-024-00563-7.
[17] A. Pereira, R.O.M. Dias, D. Lourenço, M.J. Regufe, A.M. Ribeiro, A. Rodrigues, A.F. P. Ferreira, Methane and nitrogen separation by gas-SMB in activated carbon monoliths manufactured via 3D-printing, Chem. Eng. J. 512 (2025) 162315, https://doi.org/10.1016/j.cej.2025.162315.
[18] A.E. Rodrigues, C. Pereira, M. Minceva, L.S. Pais, A.M. Ribeiro, A. Ribeiro, M. Silva, N. Graça, J.C. Santos, Simulated Moving Bed Technology: Principles, Design and Process Applications, Butterworth-Heinemann, Oxford, 2015.
[19] A. LaCava, K. McKeigue, Continuous pressure difference driven adsorption process, Messer LLC, 1996 (Patent Number: US5487775A).
[20] R.D. Rothchild, Gas separation by continuous pressure-swing chromatography, Individual. Patent Number: US5672197A (1997).
[21] L.S. Cheng, S.T. Wilson, Process for Separating Propylene from Propane, Honeywell UOP LLC, 2001 (Patent Number: US6293999B1).
[22] L.S. Cheng, S.T. Wilson, Vacuum Swing Adsorption Process for Separating Propylene from Propane, Honeywell UOP LLC, 2001 (Patent Number: US6296688B1).
[23] D.P. Rao, S.V. Sivakumar, S. Mandal, S. Kota, B.S.G. Ramaprasad, Novel simulated moving-bed adsorber for the fractionation of gas mixtures, J. Chromatogr. A 1069 (1) (2005) 141–151, https://doi.org/10.1016/j.chroma.2004.08.078.
[24] K.P. Kostroski, P.C. Wankat, Separation of dilute binary gases by simulated-moving bed with pressure-swing assist: SMB/PSA processes, Ind. Eng. Chem. Res. 47 (9) (2008) 3138–3149.
[25] K.P. Kostroski, P.C. Wankat, Separation of concentrated binary gases by hybrid pressure-swing adsorption/simulated-moving bed processes, Ind. Eng. Chem. Res. 48 (9) (2009) 4445–4465.
[26] Z. Qian, Y. Yang, P. Li, J. Wang, A.E. Rodrigues, An improved vacuum pressure swing adsorption process with the simulated moving bed operation mode for CH4/N2 separation to produce high-purity methane, Chem. Eng. J. 419 (2021) 129657, https://doi.org/10.1016/j.cej.2021.129657.
[27] Z. Qian, Y. Zhou, Y. Yang, P. Li, Methane recovery from low-grade unconventional natural gas by the integrated mode of the conventional/improved vacuum pressure swing adsorption processes, Fuel 331 (2023) 125717, https://doi.org/10.1016/j.fuel.2022.125717.
[28] Z. Qian, Y. Zhou, Y. Yang, P. Li, CH4/N2 adsorptive separation by a ZSM-5 zeolite packed multicolumn VPSA process with the SMB operation mode for high-purity methane production, Ind. Eng. Chem. Res. 62 (20) (2023) 7987–8001, https://doi.org/10.1021/acs.iecr.3c00187.
[29] Y. Miao, Z. Qian, H. Cao, Y. Yang, P. Li, Modelling and experiment for simultaneous biogas upgrading and CO2 capture by an advanced VPSA-SMB process, Chem. Eng. Sci. 307 (2025) 121371, https://doi.org/10.1016/j.ces.2025.121371.
[30] F.A. Da Silva, J.A. Silva, A.E. Rodrigues, A general package for the simulation of cyclic adsorption processes, Adsorpt 5 (3) (1999) 229–244, https://doi.org/10.1023/a:1008974908427.
[31] R.B. Bird, W.E. Stewart, E.N. Lightfoot, Transport Phenomena, John Wiley & Sons, 2007.
[32] N. Wakao, T. Funazkri, Effect of fluid dispersion coefficients on particle-to-fluid mass transfer coefficients in packed beds: correlation of Sherwood numbers, Chem. Eng. Sci. 33 (10) (1978) 1375–1384, https://doi.org/10.1016/0009-2509(78)85120-3.
[33] N. Wakao, S. Kaguei, T. Funazkri, Effect of fluid dispersion coefficients on particle-to-fluid heat transfer coefficients in packed beds: correlation of nusselt numbers, Chem. Eng. Sci. 34 (3) (1979) 325–336, https://doi.org/10.1016/0009-2509(79)85064-2.
[34] L.-K.P. Hsu, H.W. Haynes Jr., Effective diffusivity by the gas chromatography technique: analysis and application to measurements of diffusion of various hydrocarbons in zeolite NaY, AICHE J. 27 (1) (1981) 81–91, https://doi.org/10.1002/aic.690270113.
[35] M. Mazzotti, G. Storti, M. Morbidelli, Robust design of countercurrent adsorption separation: 3. Nonstoichiometric systems, AICHE J. 42 (10) (1996) 2784–2796, https://doi.org/10.1002/aic.690421010.
[36] V.I. Águeda Maté, J.A. Delgado Dobladez, S. Álvarez-Torrellas, M. Larriba, Á. Martínez Rodríguez, Modeling and simulation of the efficient separation of methane/nitrogen mixtures with [Ni3(HCOO)6] MOF by PSA, Chem. Eng. J. 361 (2019) 1007–1018, https://doi.org/10.1016/j.cej.2018.12.154.
[37] G. Xiao, T.L. Saleman, Y. Zou, G. Li, E.F. May, Nitrogen rejection from methane using dual-reflux pressure swing adsorption with a kinetically-selective adsorbent, Chem. Eng. J. 372 (2019) 1038–1046, https://doi.org/10.1016/j.cej.2019.04.166.
[38] L. Erden, A.D. Ebner, J.A. Ritter, Separation of landfill gas CH4 from N2 using pressure vacuum swing adsorption cycles with heavy reflux, Energy Fuel 32 (3) (2018) 3488–3498, https://doi.org/10.1021/acs.energyfuels.7b03534.

[39] M. Mazzotti, G. Storti, M. Morbidelli, Optimal operation of simulated moving bed units for nonlinear chromatographic separations, J. Chromatogr. A 769 (1) (1997) 3–24, https://doi.org/10.1016/S0021-9673(97)00048-4.
[40] J.A. Delgado, V.I. Águeda, J. García, S. Álvarez-Torrellas, Simulation of the recovery of methane from low-concentration methane/nitrogen mixtures by concentration temperature swing adsorption, Sep. Purif. Technol. 209 (2019) 550–559, https://doi.org/10.1016/j.seppur.2018.07.075.
[41] Y. Wang, F. Li, Q. Hu, W. Li, D. Zhang, An improved dual-reflux pressure swing adsorption process with a novel decoupling strategy for upgrading low-quality natural gas using ETS-4, Sep. Purif. Technol. 382 (2026) 135820, https://doi.org/10.1016/j.seppur.2025.135820.